Dynamics and structural development of metamorphic core complexes

Céline Tirel, Evgenii E.B. Burov, Jean-Pierre Brun

Dynamics and structural development of metamorphic core complexes

Céline Tirel,[1,2] Jean-Pierre Brun,[1] and Evgueni Burov[3]

Received 15 February 2005; revised 10 August 2007; accepted 10 October 2007; published 8 April 2008.

[1] The development of metamorphic core complexes (MCCs) in a thickened continental lithosphere is studied using fully coupled thermomechanical numerical code, accounting for elastic-brittle-ductile properties of constituent rocks. For MCCs to develop, the middle lower crust and the sub-Moho mantle are required to be weak enough to flow laterally, so as to simultaneously feed the exhuming dome and enable the Moho to keep a flat geometry. The conditions are satisfied with initial Moho temperatures of 800°C or higher, with crustal thicknesses of 45 km or greater, and with initial effective viscosities lower than 10^{20} Pa s and 10^{22} Pa s in the lower crust and the underlying mantle, respectively. A compositional (mainly density) anomaly with the properties of granite is placed centrally in the crust to localize strain at the onset of deformation. During a first stage of ''upper crust necking,'' the deformation pattern is relatively symmetrical and dominated by graben formation in the upper crust. When the first ductile layers reach the surface, a second stage of ''dome amplification and widening'' occurs. Dome amplification is accommodated by horizontal flow in the ductile crust, giving an early symmetrical pattern of conjugate shear zones with no obvious detachment zone. The system then rapidly becomes asymmetric, with the localization of a detachment zone along one dome limb, further accommodating dome widening. Thus the exhumation process of a metamorphic dome results in the progressive development of a detachment zone. Depending on initial Moho temperature, the detachment zone can migrate in space or die out and be replaced by a new one with an opposite dip.

Citation: Tirel, C., J.-P. Brun, and E. Burov (2008), Dynamics and structural development of metamorphic core complexes, *J. Geophys. Res.*, *113*, B04403, doi:10.1029/2005JB003694.

1. Introduction

[2] In continental orogenic domains, metamorphic core complexes (MCCs) constitute domes of deep crustal rocks exhumed and deformed during continental extension, surrounded by shallow crustal rocks that typically include sedimentary and volcanic rocks deposited (at least partly) during dome exhumation. Since their discovery in the Basin and Range of the western United States [*Davis and Coney*, 1979; *Crittenden et al.*, 1980; *Wernicke*, 1981, 1985], they have been identified in the Aegean [*Lister et al.*, 1984; *Gautier et al.*, 1990, 1993] as well as in other Alpine age mountain belts [*Dewey*, 1988] and in older orogenic belts [*Norton*, 1986; *Van Den Driessche and Brun*, 1989, 1991; *Andersen et al.*, 1991].

[3] Given their important role in the dynamics of large-scale continental extension, MCCs have been extensively studied in the field and through the use of geophysical imaging and modeling techniques. In particular, the low-angle detachment zones, which are the most striking tectonic feature of the MCCs, became the subject of a vigorous debate concerning their origin and mechanics [*Wernicke*, 1981, 1985; *Buck*, 1988; *Wernicke and Axen*, 1988; *Buck*, 1991]. Following nearly three decades of field studies (world wide review from *Dewey* [1988]; Basin and Range of western United States from *Crittenden et al.* [1980]; Caledonian belt from *Dewey et al.* [1993] and *Andersen* [1998]; Hercynian belt of western Europe from *Burg et al.* [1994]; Aegean from *Gautier et al.* [1990]; Menderes from *Bozkurt and Oberhänsli* [2001]; Tyrrhenian from *Jolivet et al.* [1998]), the main characters of MCCs can be summarized as follows. The overall structure of a MCC has a characteristic transverse size of some tens of kilometers and can even reach a hundred kilometers. The dome core, consisting of metamorphic rocks, migmatites and granite bodies, is surrounded by upper crustal units and sediments deposited during dome formation.

[4] Considering the amount of extensional displacement accommodated by a MCC and the depth of erosion, some variations must be expected. Most significantly, not all dome cores display young granite plutons or migmatized gneisses. Within the metamorphic core, the dome shaped foliation envelope can be associated with opposite senses of shear along opposite dome limbs [*Gautier and Brun*,

[1]Géosciences Rennes, UMR 6118, CNRS, Université de Rennes 1, Rennes, France.
[2]Faculty of Geosciences, Tectonophysics, Utrecht University, Utrecht, Netherlands.
[3]Laboratoire de Tectonique, UMR 7072, CNRS, Université Pierre et Marie Curie, Paris, France.

0148-0227/08/2005JB003694$09.00

1994a]. However, the majority of MCCs show a uniform sense of shear from one limb to the other, with finite strain intensities usually higher in the detachment zone, as demonstrated by the presence of C/S mylonites [*Davis*, 1987; *Lister and Davis*, 1989; *Jolivet et al.*, 1998]. Because of the cooling during the dome rise, the brittle-ductile transition is likely to migrate downward with respect to the exhuming dome, as shown by the complex superposition of brittle deformation on ductile fabrics observed in most MCCs [*Davis*, 1987; *Lister and Davis*, 1989; *Brun and Van Den Driessche*, 1994]. In the detachment zone, high-temperature mylonites are sometimes seen to be reworked into cataclasites and breccias [*Davis*, 1987].

[5] In the present paper, the term ''detachment zone'' describes the whole normal sense shear zone that separates, from brittle upward to ductile downward, the metamorphic dome (i.e., the metamorphic core complex proper) from the hanging wall and overlying sediments. This is in agreement with the earliest conceptual models for extensional detachment developed by *Davis* [1983, 1987], *Wernicke* [1985], *Davis et al.* [1986], or *Lister and Davis* [1989]. On the basis of the outcomes of careful field observations, some authors have found it pertinent to emphasize the difference between the low-angle detachment faults where development is restricted to the brittle crust and the ductile shear zones to which they are connected at depth (see, in particular, *Lister and Davis* [1989]).

[6] The longstanding debate regarding the origin of low-angle detachments has brought about two opposing theoretical explanations. First, the ''simple shear model'' [*Wernicke*, 1981, 1985] postulates that detachments initiate as low-angle normal faults through the whole crust, with dips lower than 30°. In addition, this model has been modified to incorporate specific structural features, for example, footwall arching [*Spencer*, 1984] and development of multiple and sequential detachment [*Lister and Davis*, 1989]. Conversely, the ''rolling hinge model'' [*Buck*, 1988; *Hamilton*, 1988; *Wernicke and Axen*, 1988; *Wdowinski and Axen*, 1992; *Axen and Bartley*, 1997] considers that detachments originate from the sequential development of high-angle normal faults. This model suggests that with increasing extension, the isostatic footwall uplift migrates with the withdrawing hanging wall; high-angle normal faults are rotated to low dips and then abandoned as a new fault develops in the hanging wall. At a finite amplitude of displacement, this process creates a flat-lying detachment. Whereas the simple shear model is not easy to reconcile with Anderson's theory of faulting [*Anderson*, 1951; *Hubbert*, 1951] related to Mohr-Coulomb criterion of plastic failure, there are a number of authors who have suggested a range of plausible explanations for this, from various strong friction-softening mechanisms to rotation of local stress/strain axes [*Livaccari et al.*, 1995; *Wills and Buck*, 1997; *Westaway*, 1999; *Lavier et al.*, 2000]. These assumptions are sustained by some studies which show low-angle normal faulting activity (with dip less than 35°) [*Rigo et al.*, 1996; *Abers et al.*, 1997].

[7] The underlying flat Moho geometry below MCCs (Basin and Range from *Allmendinger et al.* [1987] and *Hauser et al.* [1987] and Aegean from *Makris* [1978], *Sachpazi et al.* [1997], and *Tirel et al.* [2004b]) is an important constraint for dynamic interpretation, despite the lack of precise information on the timing of flat Moho development. As argued by *Block and Royden* [1990], *Buck* [1991] and, more recently, by *McKenzie et al.* [2000] the evidence for a flat Moho requires ductile crustal flow at the regional scale. This is favored in areas where the continental crust was previously thickened and thermally relaxed, leading to Moho temperatures higher than 700°C [*England and Bickle*, 1984; *Gaudemer et al.*, 1988]. Lithospheric strength is then strongly reduced allowing gravitational collapse to occur [*Sonder et al.*, 1987; *Ranalli*, 1997]. Thermal relaxation following thickening [*England and Thompson*, 1986] may allow such conditions to develop but requires rather long relaxation times. However, mantle delamination [*Bird*, 1979], back-arc environments [*Hyndman et al.*, 2005] or slab detachment [*Gerya et al.*, 2004], triple junction interaction or hot spot migration [*Wakabayashi*, 2004] provide other possibilities where strong thermal weakening of the crust and mantle can occur. This concept of MCC development in a thickened crust involving a thick and weak ductile layer able to flow horizontally is already incorporated in the conceptual model known as ''fluid crustal layer'' presented by *Wernicke* [1990] and has provided the basis for subsequent numerical and experimental models [*Wdowinski and Axen*, 1992; *Brun et al.*, 1994; *Burov and Cloetingh*, 1997; *Tirel et al.*, 2006].

[8] In most available field studies and models, the emphasis is put on the detachment zone itself and little attention is given to the MCC proper, i.e., the exhumed metamorphic dome. Consequently, the exact nature of the relationship between the detachment zone and the MCC remains an open question. More precisely, it is generally assumed that the detachment zone initiates at an early stage of extension and that, in the following, it controls the exhumation of the ductile crust. Unfortunately, there is little, if any, direct evidence to support this proposition and as such this subject merits further investigation. Although it is well agreed that there is a necessity for ductile crustal flow to have occurred on a regional scale, the nature of the relationship between the kinematics of deformation at the surface (as it is portrayed from field studies) and the deformation processes occurring in the middle lower crust is poorly understood. Indeed, little is known about the dynamics, structure and deformation pattern of MCCs at the crustal and lithosphere scales. This study seeks to address these issues using lithosphere-scale thermomechanical models.

[9] In this paper, a first series of numerical experiments is used to calibrate the models, in terms of initial crustal thickness and mantle heat flux. A second set of numerical experiments is used to determine the combination of boundary velocities and initial Moho temperatures suitable for the development of MCCs. These models simulate the asymmetric extension of a ''hot lithosphere,'' with a 60 km thick crust and Moho temperatures in the range 710–1310°C. In both series, a density-viscosity anomaly is placed within the ductile crust at the model center to favor localization of deformation. To be able to carry out a parameter study, it was also necessary to trigger deformation at the same place (at the model center) and at the same time (at the beginning of the experiment) in all models to allow comparison. The models describe the evolution of progressive deformation and thermal state at the crustal scale. The results illustrate

the initial necking of the upper crust, the shape evolution of exhuming metamorphic domes, crustal-scale ductile flow patterns and the geometry and distribution of shear zones including detachments. The results are used to develop a new model for MCCs and their associated detachment faults and to determine under what conditions –regarding the thermomechanical state of the lithosphere they can form. The variability of detachments is discussed in terms of location, vergence and stability in time.

2. Thermal-Mechanical Modeling

2.1. Model Design, Rheology Structure, and Initial and Boundary Conditions

2.1.1. Model Geometry

[10] The model (Figure 1) geometry comprises a rectangular box (400 × 100 km) composed of a 60 km thick continental crust lying above a 40 km thick lithospheric mantle. The numerical grid is made of 200 × 50 quadrilateral bilinear elements (2 km × 2 km). Each element is subdivided into two pairs of triangular subelements to avoid mesh locking [*Cundall*, 1989].

2.1.2. Boundary and Initial Conditions

[11] It can be considered that large-scale extension domains result from gravitational spreading of a hot and weak lithosphere. However, extension of the entire lithosphere is necessarily dependent on displacements applied at plate boundaries. In the case of the Aegean, for example, extension in the overriding plate results from the rollback of the African slab at the South Hellenic subduction zone [*Le Pichon*, 1982; *McClusky et al.*, 2000]. For consistency with natural systems, e.g., Basin and Range of western United States and the Aegean domain, a horizontal displacement with a constant velocity is applied to one lateral boundary of the model (to the left in Figure 1a), the opposite boundary being fixed. In vertical direction, free-slip conditions are applied at both sides of the model (naturally, these free-slip conditions are constrained by the bottom boundary conditions). The model surface was left free (no conditions on stress or displacement). The bottom boundary condition is represented by a pliable Winkler basement, which implies free slip in horizontal direction and vertical normal stresses proportional to the vertical displacement of the boundary [*Burov and Cloetingh*, 1997]. These stresses were chosen to be proportional to the density contrast between the bottom of the model and the underlying mantle, which corresponds to the local isostatic compensation. It is noteworthy that the Moho interface is free to move or to deform during the experiment. For the initial thermal field, four conductive geotherms G1 to G4 (Figure 1b) are tested, corresponding to four different values of mantle heat flux that cover a likely range of initial thermal conditions. The surface temperature is fixed at 0°C and zero heat flow (no heat exchanges with the surrounding region) is set as the lateral thermal boundary condition. Strength profiles S1 to S4 corresponding to geotherms G1 to G4 for a boundary velocity of 0.66 cm a^{-1} (which yields geodynamically representative bulk strain rate on the order of 5.5×10^{13} s^{-1}) are shown in Figure 1c. In all profiles except S1, the mantle is entirely ductile and low to very low strength. Among the other controlling parameters, the numerical time step is limited by the minimal Maxwell time of the system. Thus, to handle numerical instabilities while keeping the computations within reasonable time limits, it was necessary to assign the lower and upper effective viscosity cutoffs (5×10^{19} and 10^{26} Pa s, respectively). This range is comparable with the lithospheric effective viscosity range, and the lower viscosity is sufficiently small to allow for crustal flow [*Burov and Cloetingh*, 1997]. Indeed, the lowermost bound on the effective crustal viscosity given by *Clark and Royden* [2000] for 70 km thick crust of the Tibetan orogen is 10^{16}–10^{18} Pa s. For 60 km thick and thinner crusts this limit is on the order of 10^{19}–10^{20} Pa s, which is compatible with our model assumptions. The initial profiles of effective viscosity (i.e., stress to strain rate ratio computed for all elastic, plastic and viscous domains) are shown in Figure 1d. Profiles P1 to P4 correspond to geotherms G1 to G4, respectively.

2.1.3. Rheological Composition, Lithology, and Choice of the Initial Perturbation

[12] The continental crust is assumed to have a quartz diorite-type composition, with a density of 2800 kg m^{-3}. In the model, three marker layers are used in order to trace the evolution of the upper, middle and lower crust; the latter is also divided into two differently colored sublayers so as to facilitate visual tracing of the developing structures. In the model, the lithospheric mantle is composed of olivine with a density of 3300 kg m^{-3}. A triangular initial density-viscosity anomaly (= granitic intrusion, Table 1), 4 km high and 80 km long, is placed at the base of the middle crust in order to trigger initial strain localization at the center of the model (see Appendix A, sections A1 to A3). The choice of a granitic intrusion for localization of deformation is justified by the fact that such contrasting intrusions are very commonly present in orogens. In theory, a low-density crustal anomaly embedded in a viscous environment may become gravitationally instable due to a Rayleigh-Taylor instability, and translate to the surface with its own rate controlled by Stokes velocity and not with a rate imposed by the regional velocity field [e.g., *Burov et al.*, 2003]. If this happens, one may fear that the density anomaly imposed in the model so as to localize initial deformation may also modify the further evolution of the model. To be certain that this is not the case, we have run a series of nine preliminary models to study the effect of such local perturbation on the modeled system (Appendix A, section A1). These experiments have demonstrated that although the size, location and density of the anomaly play a role in the system evolution, their effect on the rate of exhumation and the amount of Moho deflection is moderate. In this context, it is especially relevant to mention that our test experiments (Appendix A3) have shown that for density contrasts up to 200 kg m^{-3}, the effect of the Rayleigh-Taylor instability remains small as the strength of the brittle layer overlying the buoyant volume stays higher than the buoyancy stress associated with the density anomaly (see Appendix A, section A3, for details). Therefore we are confident that the preimposed granitic anomaly localizes stretching without significant side effects on the further evolution of the system.

[13] During the formation of a MCC, the anomaly is extremely deformed and develops a sill-like body, comparable to laccolith-type granite bodies, and is bent around the external part of the dome [*Roman-Berdiel et al.*, 1995]. In nature, laccoliths of similar size and composition can be

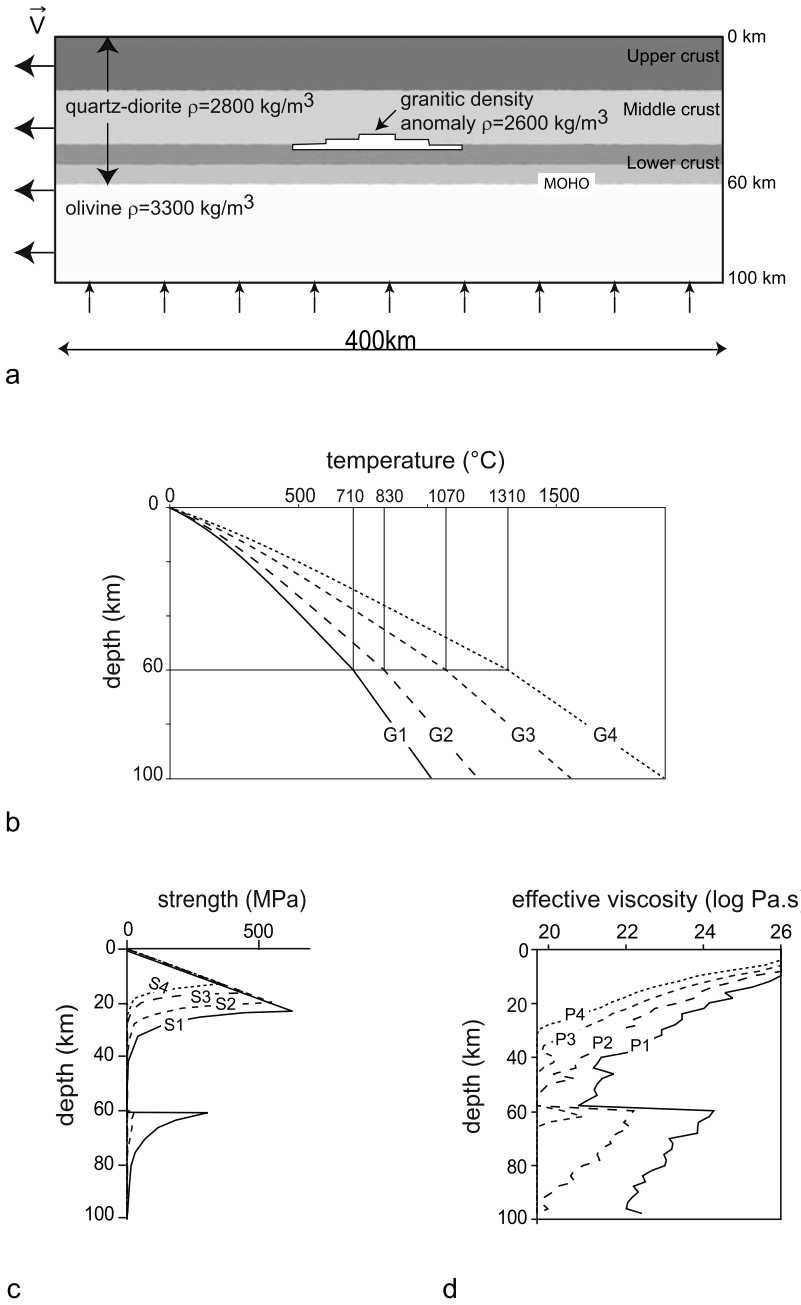

Figure 1. (a) Model geometry and velocity boundary conditions. (b) Initial geotherms G1 to G4, resulting from mantle heat flux of 25, 30, 40, and 50 m W m^{-2} and corresponding to surface heat flux of 50–60, 60–65, 70–75, and 80–90 m W m^{-2}, respectively, with lines pointing to Moho temperatures at 60 km depth. (c) Lithosphere strength profiles S1 to S4 corresponding to geotherms G1 to G4, respectively. (d) Initial effective viscosity profiles P1 to P4 corresponding to geotherms G1 to G4, respectively. The profiles of strength and effective viscosity are calculated for a boundary velocity of 0.66 cm a^{-1} yielding bulk strain rate on the order of 5.5×10^{13} s^{-1}. For model parameters, see Table 1. Note the presence of a granite-type density anomaly at the model center (see Appendix A for details). The irregularities in the effective viscosity plots mainly arise from crossing shear zones (second step of calculation).

directly observed in the Himalayas [*Lefort et al.*, 1987; *Scaillet et al.*, 1995]. Such strongly deformed sills of granites with C/S mylonite fabrics are often observed in close connection with detachment zones within MCCs [*Rehrig and Reynolds*, 1980; *Reynolds and Rehrig*, 1980; *Van Den Driessche and Brun*, 1991; *Gautier et al.*, 1993; *Gautier and Brun*, 1994b, 1994a]. Moreover, on the basis of field evidence in Papua New Guinea [*Hill et al.*, 1992; *Baldwin et al.*, 1993], *Lister and Baldwin* [1993] suggested that the formation of MCCs may be triggered by plutonic

Table 1. Variables and Parameters Used in Models

	Values and Units	Comments
	Variables	
Initial crustal thickness C_{thick}	30, 45, 60 km	continental crust
Boundary velocity V	0.33, 0.66, 1, 1.32, 2, 2.66 cm a^{-1}	applied on left side
Mantle heat flux MHF	25, 30, 40, 50 mW m^{-2}	applied geotherms
Initial Moho temperature T_{Mi} for C_{thick} = 60 km	710, 830, 1070, 1310°C	calculated temperatures
Initial Moho temperature T_{Mi} for C_{thick} = 45 km	580, 670, 860, 1040°C	calculated temperatures
Initial Moho temperature T_{Mi} for C_{thick} = 30 km	450, 510, 640, 770°C	calculated temperatures
	Parameters	
Power law constant A_1	1.26×10^{-3} MPa^{-n} s^{-1}	quartz-diorite (crust)
Power law constant n_1	2.4	quartz-diorite (crust)
Creep activation energy E_{a1}	219 kJ mol^{-1}	quartz-diorite (crust)
Power law constant A_2	1.25×10^{-9} MPa^{-n} s^{-1}	granite (anomaly)
Power law constant n_2	3.2	granite (anomaly)
Creep activation energy E_{a2}	123 kJ mol^{-1}	granite (anomaly)
Power low constant A_3	7×10^{4} MPa^{-n} s^{-1}	olivine (mantle)
Power law constant n_3	3	olivine (mantle)
Creep activation energy E_{a3}	520 kJ mol^{-1}	olivine (mantle)
Density ρ_1	2800 kg m^{-3}	crust
Density ρ_2	2600 kg m^{-3}	anomaly of granite
Density ρ_3	3300 kg m^{-3}	mantle
Thermal conductivity k_1	2.5 W m^{-1} K^{-1}	crust
Thermal conductivity k_2	3.3 W m^{-1} K^{-1}	mantle
Coefficient of thermal expansion α	3×10^{-5} K^{-1}	
Internal heat production at surface H_s	10^{-9} W kg^{-1}	
Production decay depth h_r	12 km	

activity during episodes of continental extension. Interestingly, it should be noted that a number of conceptual models of MCCs formation also postulate the presence of laccolith/sills granitic bodies in the middle of the crust, prior to the dome development [e.g., see *Norlander et al.*, 2002, Figure 8].

[14] Crustal thickening induced metamorphism, which apparently precedes large-scale extension, like in the Basin and Range Province in the western United States or in the Aegean, may enhance the decrease of crustal density with depth. As suggested by *Gerya et al.* [2001], this can lead to gravitational instability due to changes in mineral assemblages and the thermal expansion of minerals. Such density changes and related buoyancy effects have not been taken into account in the calculations presented here, except in the numerical experiments with the local anomaly placed at the center of the models.

2.1.4. Implementation of Viscoelastoplastic Constitutive Laws

[15] The rheology of the materials in the model is nonlinear brittle-elastic-ductile (Table 1). Material parameters for ductile creep are obtained from *Ranalli and Murphy* [1987] for the quartz diorite, *Kirby and Kronenberg* [1987] for the granite intrusion, and *Brace and Kohlstedt* [1980] for olivine (Table 1). Ductile creep is described by an experimental uniaxial power law relationship between strain rate and stress [*Kirby and Kronenberg*, 1987]:

$$\dot{\varepsilon} = A_0(\sigma_1 - \sigma_3)^n \exp(-H/RT), \tag{1a}$$

where $H = E_a + PV$; $\dot{\varepsilon}$ is the strain rate; T is the temperature in K, σ_1 and σ_3 are the principal Cauchy stresses (compression is negative); P is the pressure; V is the activation volume; A_0, H, E_a, and n are the material constants (Table 1); and R is the universal gas constant. Inside the numerical code, the uniaxial relationship (1a) is converted to a triaxial form using geometrical proportionality factors [e.g., *Burov et al.*, 2003]. This is needed because the rotations due to deformation can be large, and hence the invariant form of stress tensor has to be used:

$$\dot{\varepsilon}_{ij} = A^*\left(\mathrm{Inv}_{\mathrm{II}}(\sigma_{ij})\right)^{1/2}\sigma_{ij}^{n-1}\exp(-H/RT), \tag{1b}$$

where $\mathrm{Inv}_{\mathrm{II}}(\sigma_{ij}) = \sigma_{\mathrm{II}}^{\mathrm{dev}}$ is the second stress invariant, or effective shear stress, and $A^* = \frac{1}{2}A_0 3^{(n+1)/2}$. Equation (1b) is then used to compute instantaneous effective viscosity μ_{eff}:

$$\mu_{eff} = \left[\left(\mathrm{Inv}_{\mathrm{II}}\dot{e}_{ij}\right)^{1/2}\right]^{(1-n)/n}(A^*)^{-1/n}\exp\left[H(nRT)^{-1}\right], \tag{1c}$$

The referred σ_i stresses are the principal Cauchy stresses, and for the constitutive relation (1b) to be objective, these need to be corotational stresses in the Lagrangian formulation of our code (see next section).

[16] The brittle rheological term is implemented in the same way as in the FLAC algorithm [*Cundall*, 1989]. It is approximated by nonassociative Mohr-Coulomb plasticity with a friction angle $\phi = 30°$, cohesion $C_0 = 20$ MPa and dilatation angle, $\psi = 0°$, that fits the experimental Byerlee's law of frictional brittle failure [*Gerbault et al.*, 1998, 1999]:

$$|\tau| = C_0 - \sigma_n \tan\phi, \tag{1d}$$

where τ is shear stress, σ_n is normal stress. Plastic failure occurs when shear failure criterion f reaches zero and $\partial f/\partial t = 0$ [*Vermeer and De Borst*, 1984]:

$$f = \tau_{II}^* + \sigma_I^* \sin\phi - C_0\cos\phi = 0 \quad \text{and} \quad \partial f/\partial t = 0, \tag{1e}$$

where in two-dimensional formulation, $\tau_{II}^{*}=\sqrt{(\tau_{11}-\tau_{22})^2/4+\tau_{12}^2}$ and $\sigma_I^{*} = (\sigma_{11} + \sigma_{22})/2$. In terms of principal stresses, the failure criterion can be also written as $\sigma_1 - \sigma_3 = -\sin\phi(\sigma_1 + \sigma_3 - 2C_0/\tan\phi)$. The plastic flow rule $\dot{\varepsilon}_{ij}^{plas} = \lambda(\partial Q/\partial\sigma_{ij})$ is deduced from the plastic potential function $Q = \tau_{II}^{*} + \sigma_I^{*}\sin\psi$, where the unknown value of the scale multiplier λ is found from the consistency criteria $[f(\lambda) - f^{old}]/\Delta t = 0$ ("old" means the previous time step). Although the code PARAVOZ (section 2.2) handles various strain-induced softening mechanisms such as cohesion or friction angle softening, neither of these was adopted in the model presented here because the Mohr-Coulomb plasticity already has intrinsic self-localizing properties [e.g., *Gerbault et al.*, 1998] arising both from its nonassociative flow rule and partly from stress states corresponding to the corners of the Mohr-Coulomb yield surface, which, in difference from isotropic Drucker-Prager criterion, has an "edgy" shape of an hexagonal pyramid with axes $\sigma_1 = \sigma_2 = \sigma_3$ in principal stress space.

[17] The elastic behavior is described by linear Hooke's law:

$$\varepsilon_{ij} = E^{-1}\sigma_{ij} - \upsilon E^{-1}\sigma_{kk}\delta_{ij}, \tag{1f}$$

where repeating indexes mean summation and δ is Kronecker's operator. The values for the elastic moduli are $E = 80$ GPa (Young's modulus) and $\upsilon = 0.25$ (Poisson coefficient) [*Turcotte and Schubert*, 2002].

[18] The general constitutive viscoplastic model of the code is characterized by a viscoelastoplastic deviatoric behavior and an elastoplastic volumetric behavior, with following strain rate partitioning (M means Maxwell, P means "plastic"):

$$\dot{\varepsilon}_{ij} = \dot{\varepsilon}_{ij}^{M} + \dot{\varepsilon}_{ij}^{P}. \tag{1g}$$

The viscoelastic and plastic strain rate components are thus assumed to act in series. The viscoelastic constitutive law corresponds to a Maxwell component, and the plastic constitutive law corresponds to the above described Mohr-Coulomb model. In this implementation, the new global stress components are calculated, assuming that the principal directions have not been affected by the occurrence of plastic flow.

2.2. Numerical Code

[19] The large-strain thermomechanical code PAR(A)OVOZ v7-v9 used for the numerical experiments of this study is based on PARAVOZ v3 by *Poliakov et al.* [1993]. It represents a hybrid finite element/finite difference, fully explicit, time-marching Lagrangian algorithm based on the well known schema of FLAC® code [*Cundall*, 1989]. FLAC and PARAVOZ are described in detail in a host of previous studies [*Cundall*, 1989; *Poliakov et al.*, 1993; *Burov and Guillou-Frottier*, 1999; *Burov and Poliakov*, 2001; *Le Pourhiet et al.*, 2004]. Therefore we limit here the description of the code to an explanation of its basic features, and of specific differences between FLAC and PARAVOZ.

[20] The code solves the equilibrium problem for brittle-elastoductile media using general equations for Newton's second law of motion; in the continuum mechanics formulation:

$$\frac{\rho\partial v_i}{\partial t} - \frac{\partial\sigma_{ij}}{\partial x_j} - \rho g_i = 0, \tag{2a}$$

$$\frac{D\sigma}{Dt} = F(\sigma, \mathbf{u}, \nabla\dot{\mathbf{u}}, \ldots T \ldots), \tag{2b}$$

where v is velocity, ρ is density, t is time, g is acceleration due to gravity, D is material derivative and σ is Lagrangian stress, $\mathbf{u}$ stands for displacement vector, T is temperature and F denotes functional relationship. This method allows the use of a small strain formulation for large strain problems because the Lagrangian mesh is able to move and deform with the material. At each time step, the new positions of the grid nodes are calculated from the current velocity field and updated in large strain mode accounting for the rotation of principal stress axes using Jauman's corotational correction:

$$\omega_{ij} = \frac{1}{2}\left\{\frac{\partial\dot{u}_i}{\partial x_j} - \frac{\partial\dot{u}_j}{\partial x_i}\right\}$$
$$\sigma_{ij}^{corrected} = \sigma_{ij}^{small\ strain} + \left(\omega_{ik}\sigma_{kj} - \sigma_{ik}\omega_{kj}\right)\Delta t \tag{2c}$$

Solutions for velocities at mesh nodes are used to calculate element strains ε_{ij} that are employed in the constitutive relations yielding element stresses σ_{ij} and forces $\rho\partial v_i/\partial t$. The latter provide an input for the next step of calculation. In quasi-static mode, the algorithm uses artificial inertial masses to suppress inertial effects and accelerate the computations [*Cundall*, 1989]. The mechanical and constitutive equations are coupled with the heat transport equations, and the Boussinesq approximation is used to account for body forces due to thermal expansion:

$$k\nabla^2 T - \rho C_p\frac{\partial T}{\partial t} + H_r = \rho C_p\mathbf{v}\nabla T, \tag{3}$$

$$\rho = \rho_0[1 - \alpha(T - T_0)], \tag{4}$$

where $\mathbf{v}$ is the velocity vector, C_p is the specific heat, k is the thermal conductivity, H_r is the internal heat production per unit volume. α is the coefficient of thermal expansion (Table 1) used in the equation of state (4). In this study, we take into account radiogenic heating but frictional dissipation is set to zero due to the practical impossibility to constrain its efficiency. Temperature affects the thermoelastic stress, ductile stress (equations (1b)–(1c)) and body forces (equation (4)). "standard" [*Turcotte and Schubert*, 2002] exponential radiogenic heat production is used assuming common values for internal heat production at surface, $H_s = 10^{-9}$ W kg^{-1} and production decay depth, $h_r = 12$ km.

[21] The right-hand side of the equation (3) is calculated directly from the equation (2), while the left-hand side is computed using a separate numerical scheme. A dynamic relaxation technique, based on the introduction of artificial inertial masses in the dynamic system [*Cundall*, 1989], is

used to increase the internal time step and accelerate the solution of the governing equations (2).

[22] An important feature of the method relates to its capacity to handle nonlinear rheologies (temperature-, stress-, and strain- rate-dependent) and, specifically, to its capability to reproduce nonpredefined brittle shear localization [*Cundall*, 1990; *Lavier et al.*, 2000] that can be assimilated with brittle faulting. The next important feature of this method is that the code implements explicit rheological terms and is thermally coupled. By thermal coupling we mean that heat transport equations (3) are solved together with mechanical equations (2) and (4) and body forces and relevant mechanical properties are dynamically updated as function of evolving temperature. As mentioned, the code can treat thermal body forces, thermoelastic stresses, thermodynamic transformations and shear heating. However, these two last terms were switched off in our model as the energy efficiency factors and fluid content needed for their account are not well constrained. Each grid element simultaneously handles three rheological terms: brittle, elastic, and ductile; thus the local deformation mode may change from dominant brittle to dominant ductile or elastic, depending on mechanical and temperature conditions. Finally, PAR(A)OVOZ v7 benefits from a dynamic remeshing scheme, which makes it possible to process very large displacements and strains and as such, allows one to model large-displacement faults and detachment zones. Moreover, PAR(A)OVOZ v7 handles faults and detachments as shear bands, created according to Mohr-Coulomb criterion of brittle failure with a nonassociative constitutive law that corresponds to Byerlee's law [*Byerlee*, 1978].

2.3. Numerical Experiments

[23] Two series of numerical experiments were carried out (1) to calibrate the initial thermal structure and geometry and the bottom thermal and kinematic lateral boundary conditions of the models and (2) to establish a combination of parameters favorable for the development of metamorphic core complexes (Table 1 and Figures 1 and 2).

[24] The first series considers combined effects of the initial crustal thickness (C_{thick}) and mantle heat flux (MHF). Twelve models were tested with C_{thick} = 30, 45 and 60 km and MHF = 25, 30, 40 and 50 mW m^{-2}, resulting in geotherms G1 to G4 for each C_{thick} (these geotherms imply surface heat flux of 50–60, 60–65, 70–75, and 80–90 mW m^{-2}, respectively) (Figures 1b, 2b, and 2e). A horizontal displacement is applied at the left vertical boundary with V = 0.66 cm a^{-1} for each of these models. As shown in the following sections, the results of these numerical experiments suggest that an initial crustal thickness of 60 km most commonly leads to the development of MCC like features in the models and this value was therefore retained for the second series of numerical experiments (Figure 1).

[25] The second series of numerical experiments is aimed at testing the combined effect of the applied extension rate V and the mantle heat flux (MHF). A horizontal displacement is applied at the left vertical boundary with V = 0.33, 0.66, 1.00, 1.32, 2.00 and 2.66 cm a^{-1} and MHF = 25, 30, 40 and 50 mW m^{-2}, resulting in geotherms G1 to G4. These geotherms leads to initial Moho temperatures T_{Mi} = 710°C, 830°C, 1070°C and 1310°C, respectively (Figure 1b). Coupling the above parameter values for V and MHF, 24 models were computed in order to perform a parametric study. However, to facilitate understanding, the output parameters are plotted as functions of V and T_{Mi}.

[26] In section 3, Figures 3 and 9 of model structure, effective viscosity, and total shear strain correspond to those parts of the calculated grid where most of deformation is located.

3. Development of a MCC

[27] The deformation history of all models can be divided into two successive stages, namely the "upper crust necking" and the "dome amplification" [*Tirel et al.*, 2004a], illustrated here using an example with an applied extension velocity of V = 0.66 cm a^{-1} and an initial Moho temperature of T_{Mi} = 830°C (Figures 3 and 4). Taking a 40 km depth as a reference level, the dome amplification curve shows that, after a stage during which the upper crust undergoes a necking instability (Figure 3a), amplification is approximately a linear function of time until the originally ductile crust is first exhumed to the surface (Figure 4). The Moho depth curve also displays a nearly linear pattern, until the onset of ductile crust exhumation, after which the Moho depth continues to decrease but at a much lower rate (Figure 4).

[28] At an early stage of extension (4.8 Ma; Figure 3a), the upper crust develops a necking instability located above the density anomaly. The pattern of effective viscosity defines geometries that can be directly related to both structure (Figure 3a) and strain (Figure 3c). Necking is accommodated by steep conjugate normal faults, defining a symmetrical graben as illustrated by the variations of the total shear strain intensity (Figure 3c). On both sides of the graben, the upper crust remains mostly undeformed. In the middle and lower crust, the graben opening is accommodated by lateral channel flow resulting in a conjugate pattern of flat-lying shear zones (Figures 3c and 3d). Higher strain intensities are observed within the shear zones close to the Moho. These flat-lying shear zones are located in the lower and middle crust where the initial effective viscosity reaches values lower than 10^{20} Pa s.

[29] The appearance of the shear zones may be given the following interpretation. Even though ductile power law fluids cannot localize deformation in the strictest sense without additional softening, such deformation results, for high n (>2), in concentration of the flow in very narrow, high-strain rate zones, in which shear stresses rise to the levels that may locally touch the plastic yield surface, resulting in localization of brittle-plastic deformation inside the "ductile" zone. The ductile deformation concentrates near the local brittle-ductile transition boundary. The brittle-ductile transition is mainly temperature controlled: It is subhorizontal in most parts of the crust and is advected upward in the thinning portions. Advection of hot temperatures from the lower crust provides effective "softening" for the ductile part of the deformation and facilitates the concentration of deformation in ductile shear zones, a process that then leads to brittle localization.

[30] During the second stage, the dome amplifies rapidly, evidently, accelerated in part by a Rayleigh-Taylor instability due to the ascent of hot (thus less dense) material; the upper crust undergoes extreme thinning and rupture; and the dome shape rapidly becomes asymmetrical (Figure 3a).

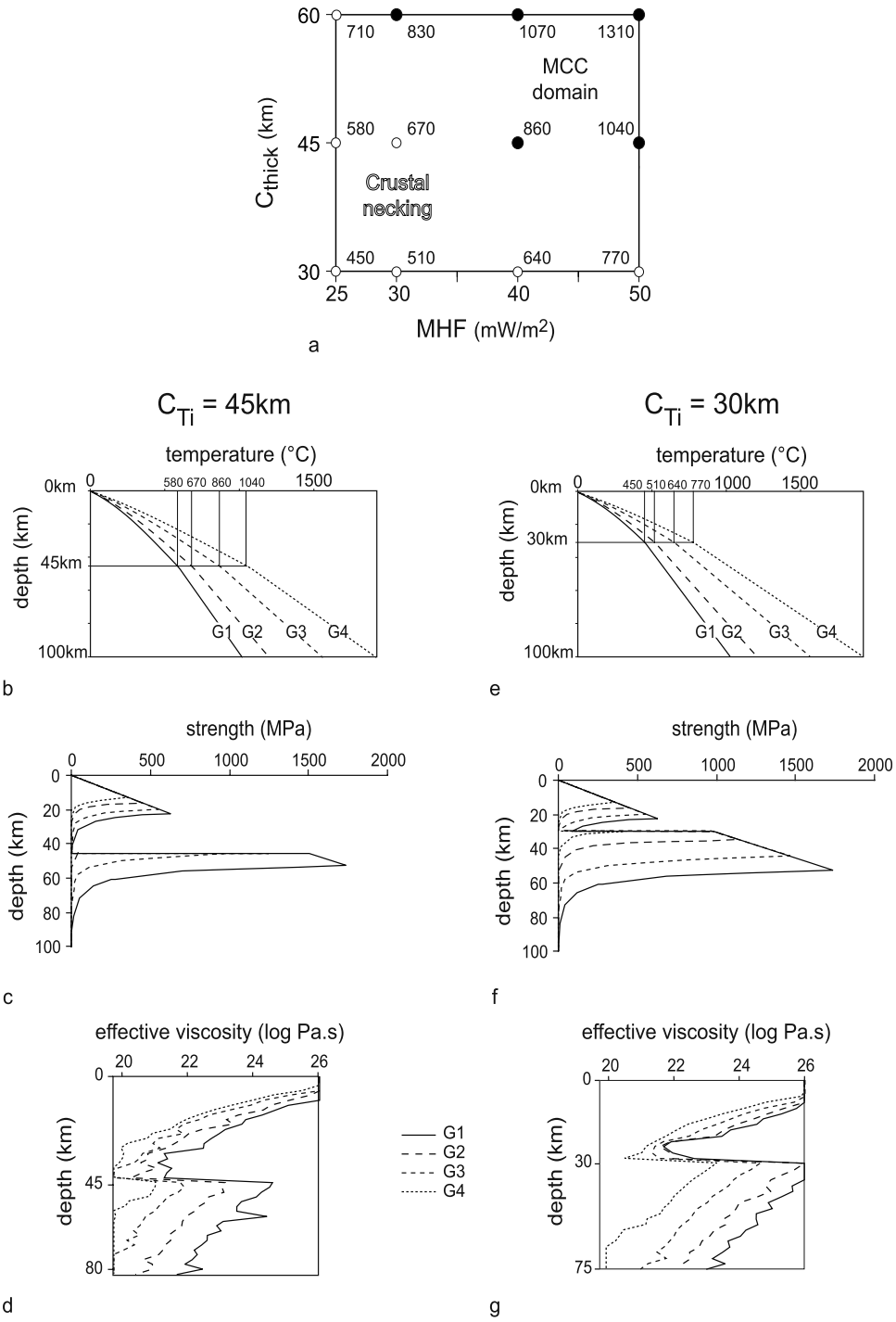

Figure 2. (a) Initial Moho temperature as a function of crustal thickness (C_{thick}) and mantle heat flux (MHF). Solid dots and open dots represent conditions favorable to the MCCs development and the whole crust necking, respectively. (b–g) Profiles of the initial geotherms G1 to G4, resulting from mantle heat flux of 25, 30, 40, and 50 m W m^{-2}; strength of the lithosphere and the initial effective viscosity for initial crustal thicknesses (C_{Ti}) of 45 km (Figures 2b, 2c, and 2d) and 30 km (Figures 2e, 2f, and 2g). The profiles of the strength and effective viscosity are calculated for a boundary velocity of 0.66 cm a^{-1} and correspond to the geotherms G1 to G4. The irregularities in the effective viscosity plots mainly arise from crossing shear zones (second step of calculation). It is noteworthy that brittle differential stresses above 500–700 MPa are most likely unrealistic as the Byerlee's law tends to overestimate rock strength at depths below 15–20 km. The rheological profiles with a crustal thickness of 60 km are devoid of this uncertainty.

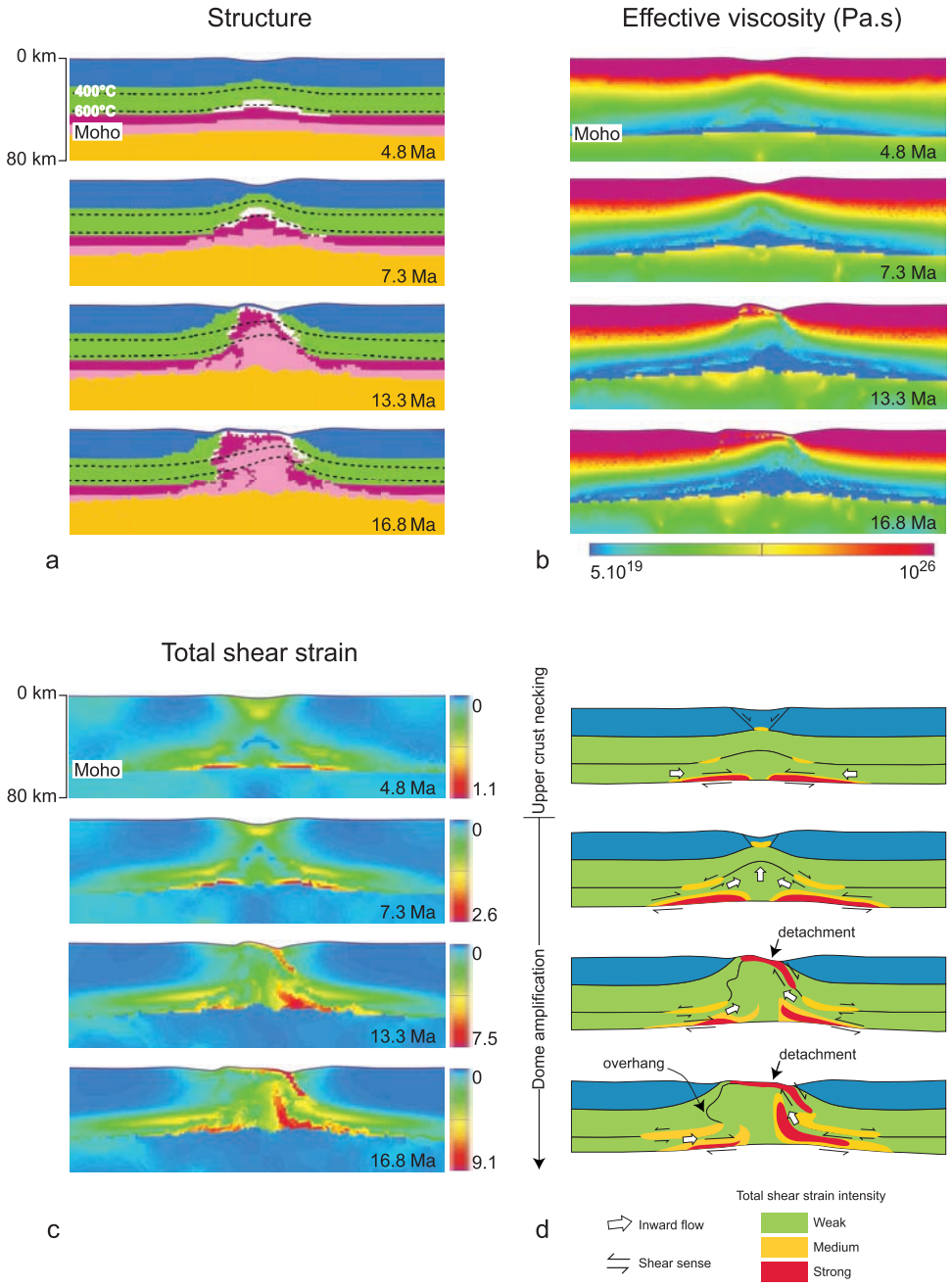

Figure 3. Sequence of sections showing the evolution of a metamorphic core complex at the lithospheric scale, with the boundary velocity V = 0.66 cm a^{-1} and the initial Moho temperature T_{Mi} = 830°C, showing the two main stages of the "upper crust necking" and "dome amplification." (a) Bulk structure and the 400°C and 600°C isotherms. (b) Effective viscosity, stress to strain rate ratio for all (brittle, elastic and ductile) domains. (c) Pattern of total shear strain. (d) Pattern of shear zones at the crustal scale. Stages of evolution are given in Ma. Structure, total shear strain, and effective viscosity representations correspond to those parts of the computed numerical mesh where most of deformation is located and not to the entire initial model.

Between 7.3 and 13.3 Ma, the middle crust reaches the surface. As the lower crustal layer rises, almost vertically, in the dome core, the middle crust undergoes layer-parallel shearing, with opposite senses of shear on the right and left dome limbs and a strong layer-perpendicular shortening.

[31] Variations in the total shear strain intensity (Figures 3c and 3d) show the evolution of the shear zone pattern that becomes progressively asymmetrical. From 4.8 to 13.3 Ma, one of the basal middle crust shear zones bends upward and connects to the zone of strain concentration at the graben base. At the evolutionary end time, this leads to a sigmoidal shear zone at the crustal scale. It is an extensional detachment zone with three main parts: flat at the dome top,

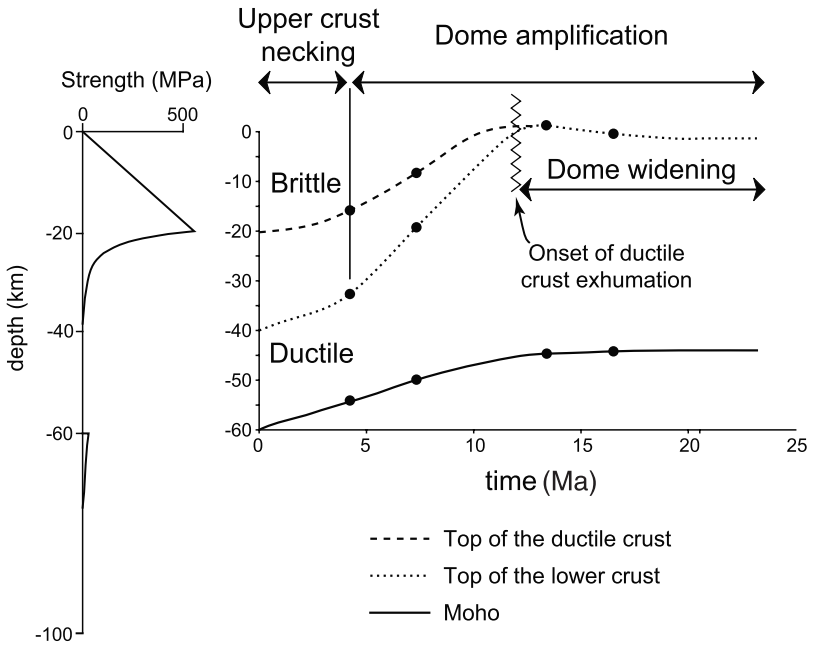

Figure 4. Lithosphere strength profile of the Figure 3 model at the onset of extension and time evolution of vertical displacements of the initial brittle-ductile transition, the top of lower crust, and the Moho.

steeply dipping along the dome limb, and flat again in the middle crust.

[32] Between 7.3 to 16.8 Ma, the dome development is characterized by an asymmetric effective viscosity pattern with a strong gradient at the dome top, as also shown by the isotherms (Figure 3a). In addition, a narrow zone of low effective viscosity coincides with the extensional detachment zone described above.

[33] An overhang develops in the dome limb opposite to the detachment zone, adding to the overall dome asymmetry (Figures 3a and 3d). This particular feature displays a close geometrical relationship with the flat-lying shear zone located in the middle crust. Above the shear zone, the upper part of the dome is transported laterally, away from the detachment zone. Below the shear zone, the lower crust flows toward the dome. As a result, the dome limb is progressively distorted at the tip of the shear zone forming an overhang at the middle crust level.

[34] Up to 7.3 Ma, the 400 and 600°C isotherms (Figure 3a) are folded in concert with structural layer boundaries and effective viscosity pattern, showing that the early stages of the evolution are nearly adiabatic (however, the issue here is probably not so much that the situation is adiabatic but that the vertical deformation velocities are so high that the thermal Peclet number is large and substantially greater than 1. Hence the heat tends to be advected upward along with the material particles). During further stages of dome widening, the middle and lower crustal interfaces are strongly advected toward the surface, within the dome, so that they are found above the 400°C and 600°C isotherms. Since the ductile-brittle transition occurs at temperatures nearing 400°C, the upper part of domes becomes cold enough to enter the brittle regime. The brittle properties of rocks are less rock-type-dependent [*Byerlee*, 1978] than the ductile properties. For this reason, this part is mechanically integrated into the upper brittle crust. During the dome widening, the geometrical pattern of the isotherms also becomes asymmetrical due to a tightening close to the detachment zone.

4. Role of the Initial Crustal Thickness

[35] We calculated 12 models, with three values of the initial crustal thickness, C_{Ti} = 30, 45 and 60 km, and four values of the mantle heat flux, MHF = 25, 30, 40 and 50 mW m^{-2}. The heat fluxes correspond to the geotherms G1 to G4 (Figures 2b and 2e). In the MHF-C_{Ti} plane, we map two distinct domains, one in which MCCs can develop and the other with crustal necking only (Figure 2a). Figures 2c, 2d, 2f, and 2g show the initial profiles of the strength and effective viscosity corresponding to the G1–G4 geotherms for C_{Ti} of 45 and 30 km. Similar profiles for C_{Ti} = 60 km are given in Figures 1c and 1d.

[36] The calculation of the brittle-ductile transition depth in these 12 models (Figure 1c, 2c, and 2f) shows that the MCC domain is characterized by a thickness of ductile crust of more than approximately 2/3 of the total crustal thickness and low viscosities in the lower crust (lower than 10^{20} Pa s) and in the underlying mantle (lower than 10^{22} Pa s).

[37] The sub-Moho mantle strength appears to have a critical role. A competent (high strength) mantle leads to lithosphere-scale necking whereas a weak (low strength) mantle is necessary for the development of MCCs, in agreement with *Buck* [1991], who showed that high Moho temperatures are a necessary requirement.

5. Dynamics of MCCs as Function of Moho Temperature and Applied Velocity

[38] Model runs were carried out over a large spectrum of initial and boundary conditions, and crucial structural and dynamic output parameters were examined. The range of velocity V applied at one of the lateral model boundaries

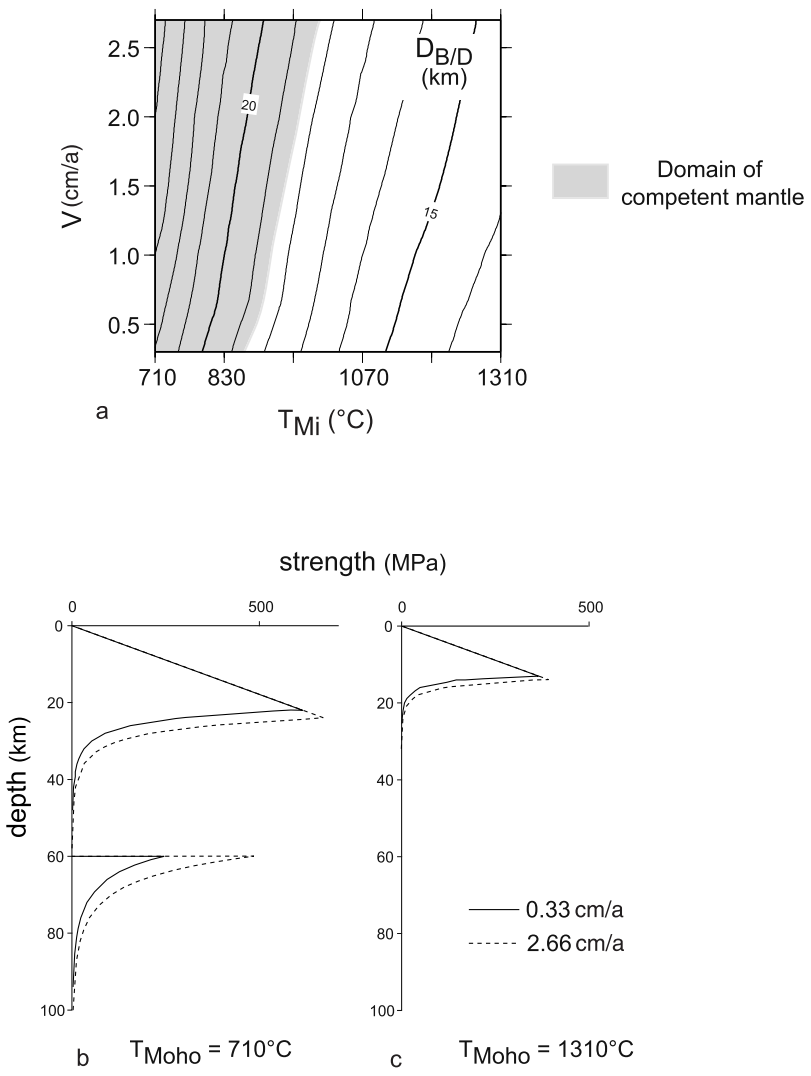

Figure 5. (a) Initial depth of the brittle-ductile transition ($D_{B/D}$) as a function of the boundary velocity and initial Moho temperature (isolines every 1 km). The domain where the sub-Moho mantle strength is higher than the ductile crust strength is shaded. (b and c) Lithosphere strength profiles for models located in the four corners of Figure 5a, with T_{Mi} = 710°C and 1310°C and V = 0.33 and 2.66 cm a^{-1}.

matches the extension rates expected to occur in nature, from 0.33 to 2.66 cm a^{-1}. The mantle heat flux was varied such that Moho temperatures at the onset of extension T_{Mi} varied from 710°C to 1310°C. Such a range of Moho temperatures includes those expected to normally occur in a 60 km thick crust. We thus expect the suite of the 24 computed models (Table 1) to be adequate for us to make geologically relevant general inferences on the development of MCCs.

[39] The output model parameters considered in the following part of this study mostly concern geometrical and/or dynamical features that can be observed and/or measured in nature, such as graben widths, timing of ductile crust exhumation, growth rate of MCCs and Moho deflection. Some other parameters that cannot be directly observed or measured in nature, like the brittle-ductile transition depth, were also studied to help the interpretation. Output parameters are plotted as functions of V and T_{Mi} and contoured using the GMT software (Generic Mapping Tools [*Wessel and Smith*, 1995]). Resulting parameter contours show some second-order variations that relate more to intrinsic model fluctuations (i.e., interactions between striction and Rayleigh-Taylor instabilities) than to uncertainties in the parameter values. Therefore more importance must be attributed to the general trends than to these second-order variations. As the absolute values of the output parameters depend on the generally poorly constrained material properties chosen for the definition of the models, they must be treated with caution. However, their relative variations are significant.

5.1. Depth of the Brittle-Ductile Transition

[40] In all numerical experiments, a single zone of brittle-ductile transition is located in the crust initially and corresponds to the major strength peak (Figure 5).

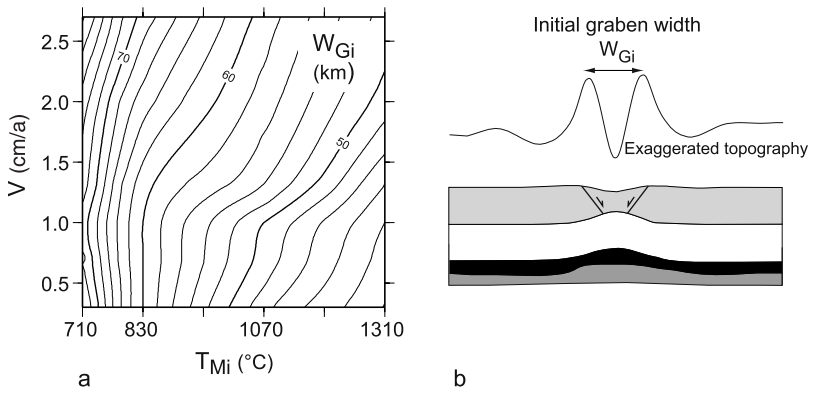

Figure 6. (a) Initial graben width (W_{Gi}) as a function of the boundary velocity (V) and initial Moho temperature (T_{Mi}), with isolines every 2 km. (b) An exaggerated topographic profile and a cross section of a model.

At T_{Mi} = 710°C strength profiles display a second strength peak that corresponds to the compositional change across the Moho (Figure 5b). With increasing temperature, this Moho strength peak disappears and the lithosphere strength is nearly entirely represented by the brittle upper crust.

[41] The depth of the brittle-ductile transition $D_{B/D}$ is located around 22–24 km at T_{Mi} = 710°C (Figure 5b) and decreases with increasing temperature to around 13–15 km at T_{Mi} = 1310°C (Figure 5c). The contoured values of the $D_{B/D}$ (Figure 5a) show that it is not only temperature-dependent but also slightly dependent on the boundary velocity. Note that the $D_{B/D}$ gradient is higher for the lower T_{Mi} values. In the domain "competent mantle" (shown in grey in Figure 5a) temperatures are low enough so that the brittle-ductile transition depths in the crust are greater than 18 km.

5.2. Initial Graben Width

[42] In all models, deformation starts with the development of a graben in the upper brittle crust (Figure 6) defined by conjugate shear bands with a dip of about 37°, which corresponds to that predicted from Mohr-Coulomb constitutive law for the plastic parameters used in this study [*Vermeer and De Borst*, 1984; *Ord*, 1991]:

$$\frac{\pi}{2} - \left(\frac{\pi}{4} + \frac{\phi + \psi}{4}\right) = \frac{\pi}{4} - \frac{\phi + \psi}{4} \approx 37^{\circ}.$$

The initial graben width W_{Gi} is measured as the distance between the two topographic highs located on graben borders (Figure 6b). The initial graben width depends on the integrated strength of the crustal layers, directly related to the depth of the brittle-ductile transition. For this reason W_{Gi} generally decreases (e.g., from 80 to 36 km), with increasing Moho temperatures and decreasing integrated strength of the lithosphere. At T_{Mi} values higher than ~830°C, W_{Gi} also increases substantially as a function of velocity, since the integral strength of the ductile layers is proportional to the strain rate.

[43] The above results indicate that the initial graben width can be considered a function of the brittle-ductile transition depth (compare Figure 6a with Figure 5a). This relationship, already pointed out by *Allemand and Brun* [1991], results from the fact that the conjugate shear zones that define the graben join each other in the brittle-ductile transition zone, at the initiation of the deformation.

5.3. Ductile Crust Exhumation and Dome Growth

[44] For practical convenience, we define the onset of the ductile crust exhumation t_{exh} as the time necessary for the layer initially located immediately below the brittle-ductile transition to reach the surface (Figure 7a). It varies from 2 to 30 Ma, mostly as a nonlinear function of the velocity V (Figure 7b). For T_{Mi} values higher than 830°C, t_{exh} shows a slight decrease with increasing temperatures, especially below V = 1.0–1.5 cm a^{-1}. For low values of T_{Mi} and high values of the velocity, t_{exh} shows a significant temperature dependence.

[45] The time necessary to exhume a 60 km wide dome (Figure 7a) is chosen here as an estimate of a critical growth time (t_{60km}). The results indicate that t_{exh} (Figure 7b) and t_{60km} (Figure 7c) have a similar dependence on the initial Moho temperature and boundary velocity. In nature, this time may be different as it is also dependent on the variable erosion rate. However, the general trends will remain unchanged [*Burov et al.*, 2003].

[46] The diagram showing the difference t_{diff} between t_{60km} and t_{exh} displays two domains of dome growth (Figure 7d). Above V = 1 cm a^{-1} t_{diff} is less than 5 Ma, indicating that a 60 km wide MCC develops during rather short geological times. Below V = 1 cm a^{-1} t_{diff} is in the range of 5–15 Ma. More generally, the comparison of t_{exh} (Figure 7b) and t_{diff} (Figure 7d) indicates that the time required to widen the dome of exposed ductilely deformed lower plate rocks to 60 km is in the range of one to two times that required to first expose the ductilely deformed rocks.

5.4. Moho Deflection

[47] The maximum upward deflection of the Moho (Md) is observed below the exhumed ductile dome. Figure 8a identifies two domains of low and high Moho deflection in models with a 60 km dome width (Figure 8b). For T_{Mi} values higher than 830°C, the Moho deflection is lower than 10 km, resulting in Moho slope values lower than 3–4°. For T_{Mi} values lower than 830°C, Moho deflection can reach

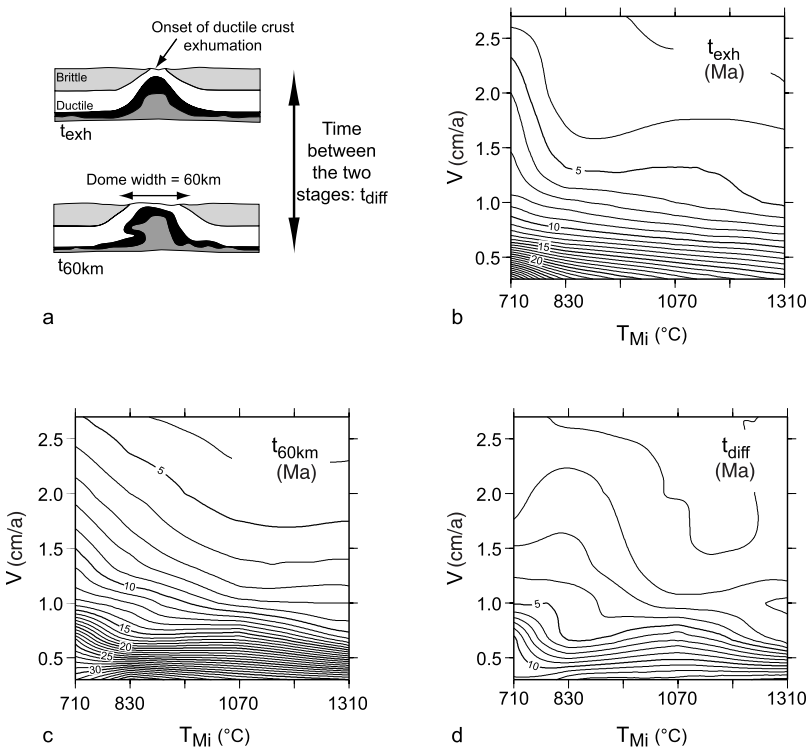

Figure 7. Critical times (in Ma) for the onset of the ductile crust exhumation (t_{exh}) and for a 60 km dome widening (t_{60km}). (a) Sketches of a model showing the onset of the ductile crust exhumation and a 60 km dome widening. (b–d) Plots of t_{exh} (Figure 7b), t_{60km} (Figure 7c), and $t_{diff} = t_{60km} - t_{exh}$ (Figure 7d) as functions of the boundary velocity V and the initial Moho temperature T_{Mi}, with isolines every 1 Ma.

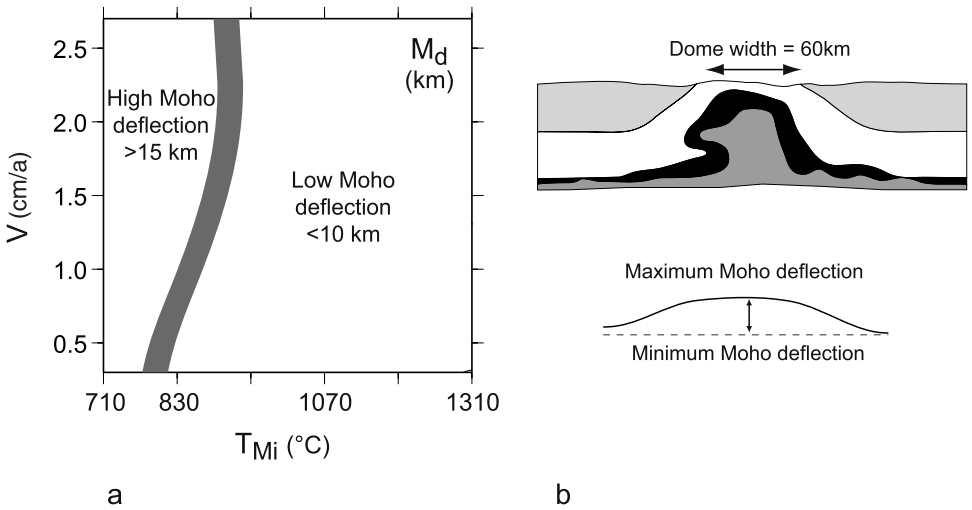

Figure 8. Moho deflection (M_d) as a function of boundary velocity (V) and initial Moho temperature (T_{Mi}) for a 60 km wide dome. (a) Diagram showing the domains of low (<10 km) and high (>15 km) Moho deflection. The domain of low Moho deflection can be considered a mapping of the V and T_{Mi} conditions that favor the development of MCCs. (b) Sketch showing how the Moho deflection is measured.

extremely high values, up to 35 km, resulting in Moho slopes in the range of 5–11°.

6. Variations in the Structural and Thermal Evolution

[48] The entire set of models computed display the same basic two-stage evolution leading to the same basic structural features, as described above for the model with V = 0.66 cm a^{-1} and T_{Mi} = 830°C (Figure 3). Variations in V and T_{Mi}, however, result in significant differences in the internal structure, strain patterns and progressive deformation, in particular, if we focus on the symmetry/asymmetry of strain patterns and their relation to boundary displacements. Therefore three other models with an initial Moho temperature T_{Mi} = 1070°C are presented here to illustrate some different trends.

6.1. Model With V = 0.33 cm a^{-1}

[49] As in all models developed in this paper, during the necking stage the base of the graben is characterized by a zone of high strain. Two other domains of high shear strain appear in the middle crust, below the graben shoulders, with a rather irregular shape (Figure 9a). At 18.1 Ma these two zones, with more regular contours, connect upward to form a bell-shaped pattern with the apex exhumed at surface and, with the limbs steeply dipping within the upper brittle crust and flat-lying below it. At this stage of the evolution, corresponding to the onset of ductile crust exhumation, the metamorphic dome is symmetrical with two opposing detachment zones of equal size. By 25.4 Ma the structure is more asymmetric; the development of the detachment on the right-hand side of the dome has ceased, and there is a single, well developed detachment on the left-hand side of the dome. The horizontal shear zones in the middle crust are more elongated. At 31.7 Ma, the bulk structure is comparable to the previous one and the dome at surface is now 60 km wide. In the middle crust, the horizontal shear zone opposite to the main detachment has propagated horizontally within the dome base.

[50] Note that the main detachment zone (Figure 9a), after an initial stage of nearly symmetrical evolution, locates along the left dome limb, toward the moving boundary and that an overhang develops at the base of the right dome limb.

[51] The isotherm pattern remains symmetrical during a large portion of the evolution. At 31.7 Ma it is asymmetrical, with a tightening close to the detachment zone.

6.2. Model With V = 1.00 cm a^{-1}

[52] Up to 8.6 Ma, the deformation pattern remains relatively symmetrical (Figure 9b) and then, as in the model with V = 0.33 cm a^{-1}, it becomes asymmetrical with a detachment zone located on the left limb of the dome. At 14.9 Ma the horizontal shear zone located in the middle crust, opposite to the detachment zone, propagates within the dome and bends upward to reach the surface to intersect the flat part of the detachment zone. Between the detachment zone and this concave-shaped shear zone, the lower ductile crust rises vertically.

[53] The overhang in the right dome limb is strongly amplified, giving a strong internal asymmetry to the dome at the crustal scale. The recumbent anticline-syncline pair on the right-hand side of the dome shares a common overturned limb that is around 60 km long. The isotherm pattern remains symmetrical up to 8.6 Ma, with bulk isotherms tightening at dome scale from the earliest stages of the evolution. The isotherm pattern becomes strongly asymmetrical at 14.9 Ma, distorted in the course of the development of the detachment zone and the upward concave shear zone.

6.3. Model With V = 2.00 cm a^{-1}

[54] The evolution of deformation is similar to that in the previous model V = 1 cm a^{-1}, except that after the stage of symmetrical evolution the detachment zone localizes on the right limb of the dome (3.5 Ma; Figure 9c). Further widening of the dome occurs along the same detachment zone (6.7 Ma) until the horizontal shear zone of the middle crust enters into the dome base and propagates toward the surface while bending upward (10.1 Ma). The upper flat-lying part of the detachment zone is then intersected, like in the model V = 1 cm a^{-1}; however, the steep section along the dome limb moved leftward, and consequently, the original detachment zone is abandoned.

[55] The overhang in the left limb already well developed at 6.7 Ma is further amplified giving the same type of reverse anticline and recumbent syncline as observed in the previous models but in the opposite dome limb (10.1 Ma; Figure 9c).

[56] Up to 6.7 Ma the thermal evolution is similar to the one described for the previous model. Then at 10 Ma the apex of the isotherms is shifted toward the dome center. This coincides with the abandonment of the early detachment zone and the propagation of the midcrustal shear zone within the dome.

7. Discussion

7.1. Applicability and Limitations of the Numerical Models

[57] The models presented in this paper provide an overview of kinematical scenarios of the development of MCCs at the crustal and lithospheric scales. They show that,

Figure 9. Evolution in time (in Ma) of the structure, the 400–600°C isotherms and the variation of total shear strain of three models with T_{Mi} = 1070°C and three different boundary velocities: (a) V = 0.33 cm a^{-1}, (b) V = 1 cm a^{-1}, and (c) V = 2 cm a^{-1}. The major detachment zone is located along the right limb of the dome in Figures 9a and 9b and along the left limb in Figure 9c. The three models present a reverse anticline and a recumbent syncline in the ductile crust, in the dome limb opposite to the detachment zone. The major horizontal shear zone located in middle crust to the right side of the model propagates inside the dome core (in Figure 9b at 14.9 Ma and in Figure 9c at 10.1 Ma). Structure and total shear strain representations correspond to those parts of the computed numerical mesh where most of deformation is located and not to the entire initial model.

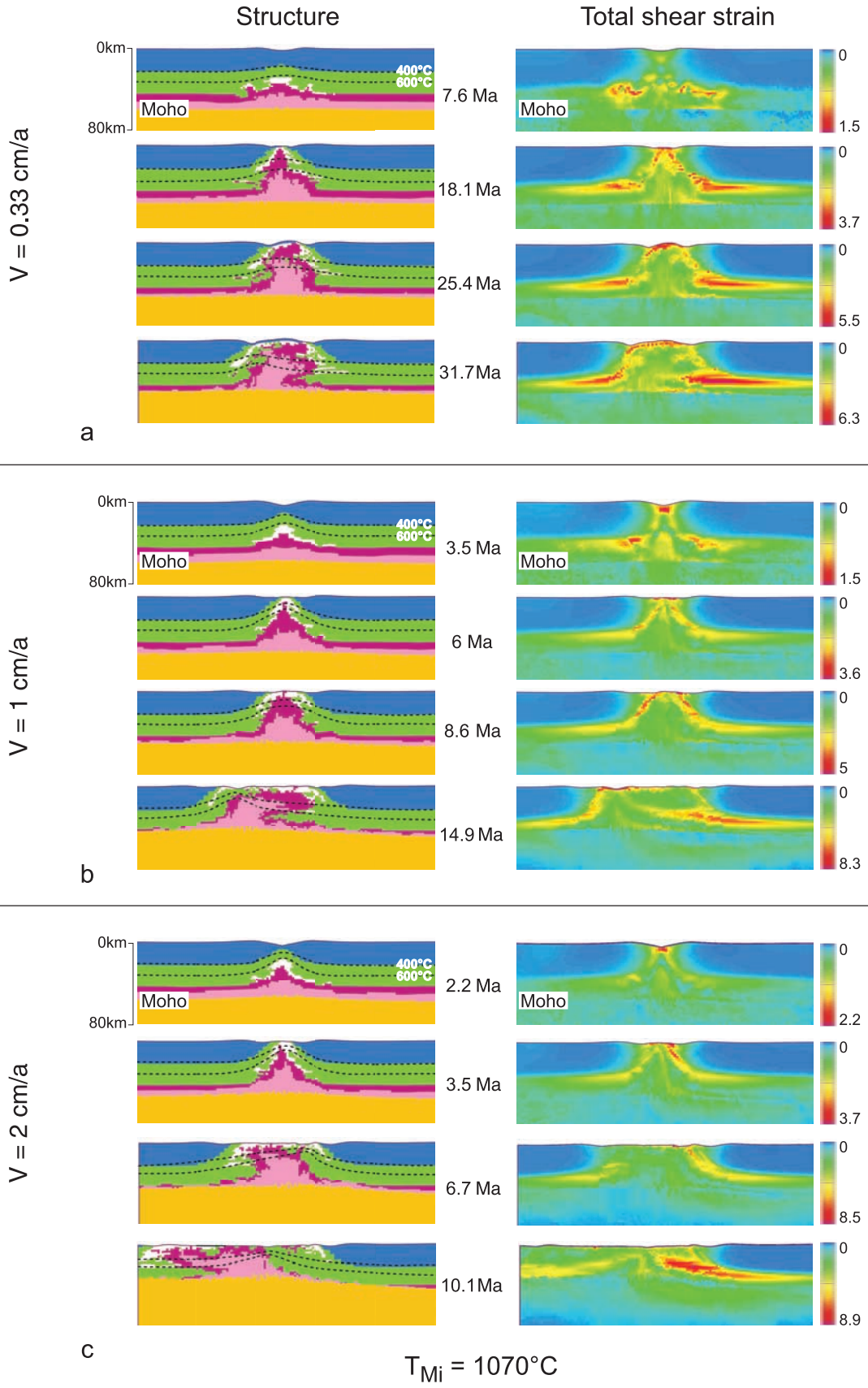
Structure
Total shear strain
V = 0.33 cm/a
0km
80km
400°C
600°C
Moho
7.6 Ma
18.1 Ma
25.4 Ma
31.7Ma
0
1.5
3.7
5.5
6.3
a
V = 1 cm/a
3.5 Ma
6 Ma
8.6 Ma
14.9 Ma
3.6
5
8.3
b
V = 2 cm/a
2.2 Ma
3.5 Ma
6.7 Ma
10.1Ma
8.5
8.9
c
T_{Mi} = 1070°C

Figure 9

even for extremely simple initial conditions, a large variety of configurations can develop as a function of the initial crustal thickness, initial Moho temperature and applied boundary velocity. We thus suggest that there is no single MCC pattern applicable to all natural examples.

[58] At a basic level, the MCC-like structures that develop in the models can be compared to those found naturally in terms of thermal and structural history and critical time of development. The models feature (1) units of initially ductile crust that become progressively cooler and enter into the brittle field as they are exhumed during extension; (2) a generally domal structure for the exhumed lower and middle crust with a detachment zone well developed on one limb; and (3) development times similar to those inferred from geological observations with domes attaining a width of 60 km at the surface in 5 to 35 Ma. Such characteristics are commonly observed in the Basin and Range of the western United States [*Davis and Coney*, 1979; *Crittenden et al.*, 1980; *Wernicke*, 1981; *Miller et al.*, 1983; *Wernicke*, 1985; *McCarthy et al.*, 1991; *Kruger and Johnson*, 1994; *Carter et al.*, 2004], the Aegean [*Gautier et al.*, 1993; *Gautier and Brun*, 1994a; *Jolivet et al.*, 1994], the Tyrrhenian [*Jolivet et al.*, 1998] or the Betics [*Vissers et al.*, 1995; *Martinez-Martinez et al.*, 2004], as well as in older orogens like the Caledonides [*Norton*, 1986; *Andersen et al.*, 1991] or the Hercynides [*Van Den Driessche and Brun*, 1991; *Burg et al.*, 1994].

[59] In the models, the critical time of exhumation is slightly accelerated by the low density of the assumed anomaly (compare Appendix A, section A1). However, note that variations in size, density and location of the anomaly do not change the order of magnitude of the observed critical times and the range of critical times for exhumation predicted by the models (2 and 15 Ma) are compatible with the values obtained for natural examples [*Dallmeyer et al.*, 1986; *Anderson et al.*, 1988; *Gautier et al.*, 1993; *Gautier and Brun*, 1994b; *John and Howard*, 1995; *Vanderhaeghe et al.*, 2003; *Carter et al.*, 2004].

[60] There are three main limitations inherent to our lithosphere-scale numerical modeling. First, even if the brittle rheology used for the model upper crust is of Mohr-Coulomb type, the code developed in this paper (along with other geodynamic codes) is not able to simulate the development of 'true' discontinuous frictional faults. Faults produced in the models are instead similar to shear bands, which do, however, have the same dip angles as real normal faults would. Also, dynamic remeshing allows the simulation of large displacements on the shear bands, as if they were real faults. As a consequence, the model replicates the natural mechanics of faults and the only real difference, in comparison to nature, is that the thickness of the model "faults" is mesh-dependent and thus has no real physical significance [e.g., *Ord*, 1991]. Second, the limitation is that no particular procedure to simulate possible fault-related strain softening (e.g., friction angle softening) was adopted. Friction angle softening has never been quantified under laboratory conditions, and the application of softening in numerical models remains uncertain. However, the Mohr-Coulomb plasticity used in the code is self-localizing by itself. Third, the resolution imposed by the size of model elements (i.e., 2×2 km) means that many details observable in the field cannot be reproduced in this large-scale model. We thus refer to the "detachment zone" and do not distinguish between "detachment faults" in the brittle crust and the ductile shear zone below to which they are connected. The models presented in this paper do not reproduce deformation patterns related to the association of low-angle normal faults and ductile shear zones as commonly observed in field-scale cross sections.

[61] An important criterion for the validation of the geological applicability of the models is that they match the relatively flat Moho geometry observed below MCCs at present (Basin and Range [*Makris*, 1978; *Allmendinger et al.*, 1987; *Hauser et al.*, 1987; *McCarthy et al.*, 1991; *Kruger and Johnson*, 1994] and Aegean Sea [*Sachpazi et al.*, 1997; *Tirel et al.*, 2004b]). The evidence for a flat Moho indicates ductile crustal flow at the regional scale [*Block and Royden*, 1990; *Buck*, 1991; *McKenzie et al.*, 2000]. One uncertainty is that the precise timing of the flat Moho development is unknown and could either be during or after continental extension. Our models reproduce the Moho that shallows with the increasing amount of stretching, while remaining relatively flat, provided that the initial Moho temperature is higher than 800°C. Assuming that a deflection of up to 10–15 km over a distance of 150–200 km is the maximum acceptable for the Moho to be considered "flat", we can use the experiments for a wide range of boundary velocities (from 0.33 to 2.66 cm a^{-1}) and initial Moho temperatures (from 710 to 1310°C) in order to identify the MCC domain in the V-T_{Mi} plane.

7.2. A "Geological Window" for MCCs

[62] The models confirm the major importance of temperature and effective viscosity on the development of MCCs. As previously reported by several authors [*Block and Royden*, 1990; *Buck*, 1991; *Ranalli*, 1997] a high initial Moho temperature is necessary to allow crustal flow, a condition absolutely required for preservation of a flat Moho boundary during the development of a MCC. The models presented in this study show, for the rheology parameters chosen for the crust and mantle, that an initial Moho temperature higher than 800°C is required (Figure 8) to initiate the development of MCCs. More generally, given the temperature dependence of effective viscosity, initial effective viscosities lower than 10^{20} Pa s for the lower crust and 10^{22} Pa s for the underlying mantle are required. Models computed for different initial crustal thicknesses, from 30 to 60 km, and mantle heat flux (MHF) values, from 25 to 50 mW m^{-2}, help to define the "geological window for MCCs" (Figure 10). MCCs easily develop when the initial Moho temperature is higher than 800°C and when lower crust effective viscosity is less than 10^{20} Pa s, regardless of the crustal thickness. This excludes the development of MCCs in a "normal thickness crust" because, even for high MHF values, a Moho temperature of 800°C combined with a low effective viscosity are almost never reached. On the other hand, MCCs easily develop in a 60 km crust except if the MHF value is extremely low (25 mW m^{-2}) because the lower value of viscosity of the lower crust is typically in the order of 10^{21} Pa s.

[63] With Moho temperatures lower than 800°C the sub-Moho mantle has high strength and effective viscosity (Figure 2), resulting in strong Moho deflection and crustal-scale necking (Figure 10). In this domain, neither the

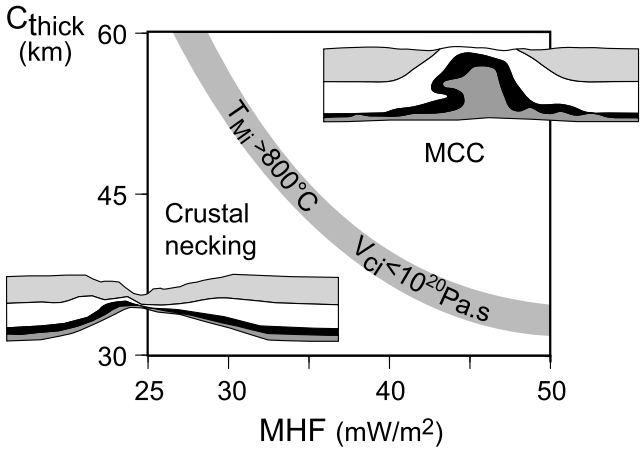

Figure 10. Domains of the MCC development and crustal necking in the coordinate system defined by the initial crustal thickness (C_{thick}) and the mantle heat flux (MHF). The boundary between the two domains roughly corresponds to an initial Moho temperature of T_{Mi} = 830°C (compare to Figure 5).

ductile crust is thick enough, nor the effective viscosity low enough to allow crustal flow. These conditions do not favor the development of MCCs.

[64] According to *McKenzie and Jackson* [2002] and *Wdowinski and Axen* [1992], lower crustal flow requires a minimum effective viscosity ratio of 50 between the sub-Moho mantle and the lower crust. In this paper we show that lower crustal flow occurs even with the effective viscosity ratio well below this value. Figures 1d and 8a show that the Moho deflection decreases with the decreasing effective viscosity contrast. At low effective viscosity contrasts, the ductile crust and sub-Moho mantle are strongly coupled and deform in a very similar fashion.

7.3. Two-Stage Development of MCCs

[65] In our models, the development of a MCC is characterized by two main stages: (1) upper crust necking and (2) dome amplification and widening. Strain is localized in and around the density-viscosity anomaly placed into the ductile crust at the center of the model.

[66] This study shows that even if the Rayleigh-Taylor effect of the anomaly is very small, the anomalies perturb the extensional strain field sufficiently for strain to localize at the model center and at the very beginning of the experiment (see Appendix A). This triggers a necking instability in the upper brittle crust. The upper crustal necking is accommodated by steeply dipping normal faults that define a symmetrical graben above the anomaly within the ductile crust. Local upper crustal thinning reduces the vertical lithostatic column and therefore induces a horizontal pressure gradient in the model. This initiates horizontal flow in the ductile crust. The second stage is a direct consequence of the upper crust necking and includes the formation and amplification of a ductile dome at the crustal scale. The assumed low-density anomaly causes very little ascending motion (its main effect is the initiation of strain localization, Appendix A, section A3). Instead, the observed upward flow below the neck area results from the gradient of horizontal pressure induced by upper crustal necking.

[67] During the early amplification and before the onset of exhumation, the vertical component of the flow rate below the upper crustal neck is significantly larger than the horizontal component due to the applied velocity field. In all models, this gives rise to the symmetrical pattern of conjugate extensional shear zones that accommodates the ductile crust exhumation at early stages, regardless of the applied boundary velocity and the initial Moho temperature.

[68] Once the initially ductile material arrives to the surface (this defines the onset of ductile crust exhumation), the strain pattern associated with dome widening becomes asymmetrical. During this late stage of the dome evolution the strain pattern, including detachment zones, becomes strongly dependent on the applied boundary velocity and the initial Moho temperature (see Figures 3 and 9).

[69] The analogue modeling of core complexes [*Brun et al.*, 1994; *Tirel et al.*, 2006] corroborates the two-stage development pattern observed in numerical models presented here as well as those of *Wijns et al.* [2005] and *Gessner et al.* [2007]. In analogue models, core complexes also result from strain localization within an initial graben in the brittle upper crust. Interestingly, the Gulf of Corinth graben is considered by *Chéry* [2001] and *Jolivet* [2001] as the initial stage of a future core complex, the evidence being the low-angle normal faulting activity, as suggested by microearthquake clustering below the graben [*Rigo et al.*, 1996]. Analogue and numerical models illustrate the close relationship between the intersection of graben normal faults and the brittle-ductile transition [*Brun et al.*, 1994; *Tirel et al.*, 2006]. The base of the graben becomes a site of strain concentration, enhancing the localization of a future detachment zone. The brittle-ductile transition thus plays a key role in the initiation and development of detachment faults, as suggested by several previous numerical modeling studies [*Melosh*, 1990; *Chéry*, 2001; *Gueydan et al.*, 2003, 2004; *Rosenbaum et al.*, 2005; *Regenauer-Lieb et al.*, 2006].

[70] Considering an ideal two-dimensional brittle layer floating on an inviscid fluid, *Lavier et al.* [1999, 2000] have shown that extension generates either multiple major faults with a small offset or a single major fault that can develop a very large offset, depending on the brittle layer thickness, cohesion, and the rate of cohesion reduction with strain. A single major fault with a large offset and an overall upward convex shape develops for small brittle layer thicknesses and a slow rate of fault weakening; this may be similar to some core complex detachments. However, as demonstrated by the above models and by previous laboratory experiments [*Brun et al.*, 1994; *Tirel et al.*, 2006], even a graben-type structure can accommodate extreme thinning of brittle upper crust, resulting in the exhumation of a gneiss dome capped by a flat-lying mylonitic detachment zone.

[71] As noted in section 7.2, the anomaly located at the model center slightly accelerates the dome rise (see also Appendix A, section A1). However, the two-stage process observed in this study is not driven by these buoyancy forces. In fact, all models undergoing localized stretching in the upper crust, i.e., development of a graben, go on to reproduce the formation of a MCC. The mechanism for dome growth relies on the occurrence of horizontal flow in

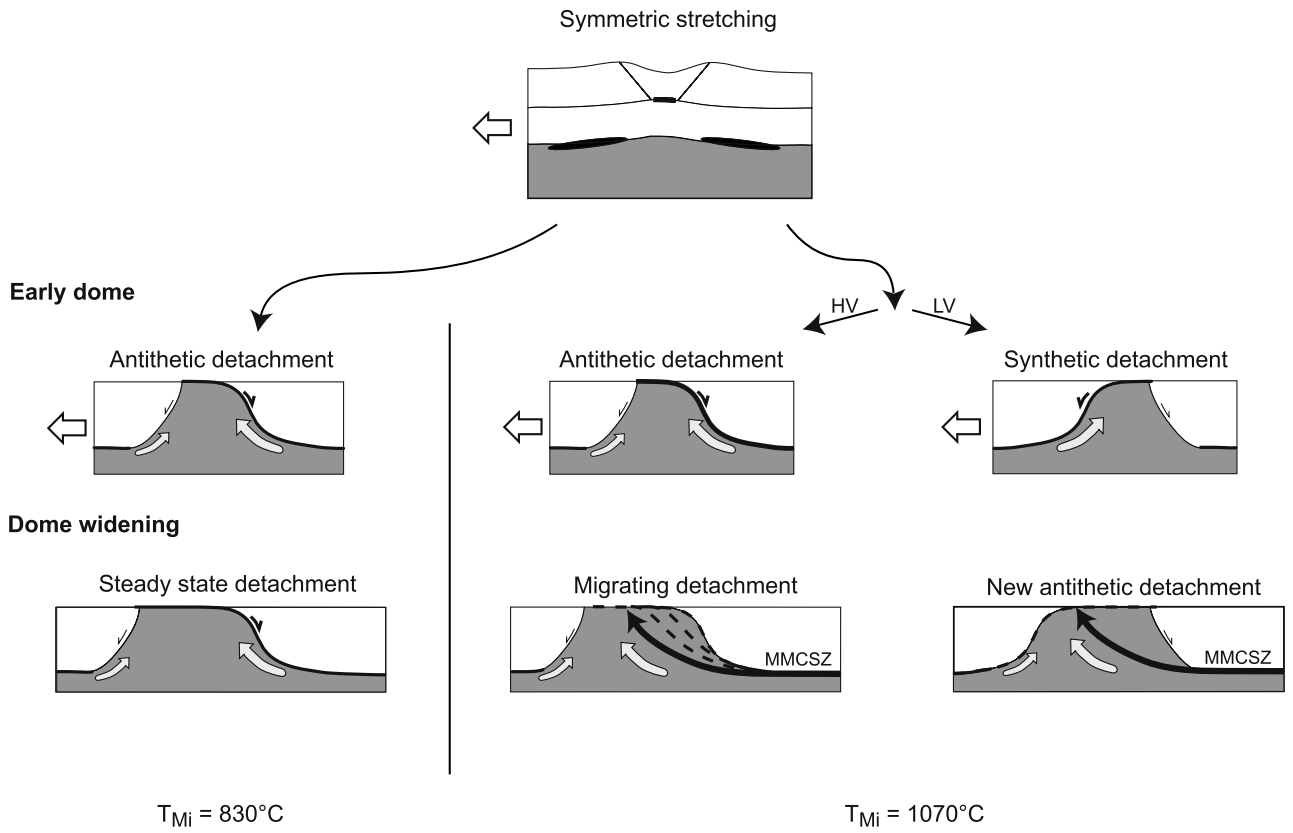

Figure 11. Main modes of the detachment zone evolution. At the first stage, the deformation pattern is close to symmetrical, with zones of high strain located at the base of a symmetrical graben, in the upper brittle crust, and in flat-lying shear zones in the ductile crust. At the second stage, a main detachment zone results from a connection between the base graben high-strain zone and one of the flat-lying shear zones in the ductile crust. With T_{Mi} = 830°C, all models show a detachment zone located on the dome limb opposite to the moving boundary. With T_{Mi} = 1070°C the main detachment zone can be located along either of the dome limbs, opposite to the moving boundary at high boundary velocities (HV) and on the side of the moving boundary at low boundary velocities (LV). At the third stage, when the dome width exceeds 60 km, the major middle crust shear zone (MMCSZ), opposite to the moving boundary, migrates within the dome core. This results in a migration of the detachment zone inside the dome: at high boundary velocities and for the initiation of a new detachment zone with an opposite dip at low boundary velocities.

the ductile crust, resulting from the horizontal pressure gradient due to upper crust thinning. Any other type of strain localization responsible for a local upper crust thinning would produce the same effect.

[72] The models show that the time required to widen the dome (of exposed ductilely deformed lower plate rocks) to 60 km is one to two times the time required to first expose the ductilely deformed rocks (Figures 7b and 7d). This indicates that the process of exhumation is accelerated from the first stage to the second stage of dome development and provides an explanation for the increase in slip rate along detachment zones observed in some MCCs. In the Harcuvar metamorphic core complex, SW Arizona, U/Th-He ages measured along a 60 km long profile parallel to the stretching direction demonstrate an abrupt change of detachment slip rate from 0.26 cm a^{-1} between circa 23 and 15 Ma, to 3.0 cm a^{-1} after circa 15 Ma [*Carter et al.*, 2004]. This increase in slip rate could be related to a two-stage evolution of the Harcuvar metamorphic core complex.

7.4. Location and Stability of Detachment Zones

[73] At an initial Moho temperature of 830°C, regardless of the imposed boundary velocity, the detachment zone localizes immediately after upper crustal necking, on the dome limb opposite to the moving boundary (e.g., Figure 3). For the asymmetric velocity field used, high temperatures advecting on the left side of the model move away from its center faster than temperatures advecting on the right side, with consequent effects on the mechanical properties and on the position of the brittle-ductile transition. The deformation becomes asymmetric, with more plastic strain on the "cold" right side in what we interpret as a detachment zone.

[74] Dome growth is accommodated by convergent lateral channel flow in the middle lower crust, resulting in a conjugate pattern of flat-lying shear zones. Higher strain intensities are found within the shear zones close to the Moho. The thermal structure becomes progressively asymmetric, with a tightening of isotherms close to the detach-

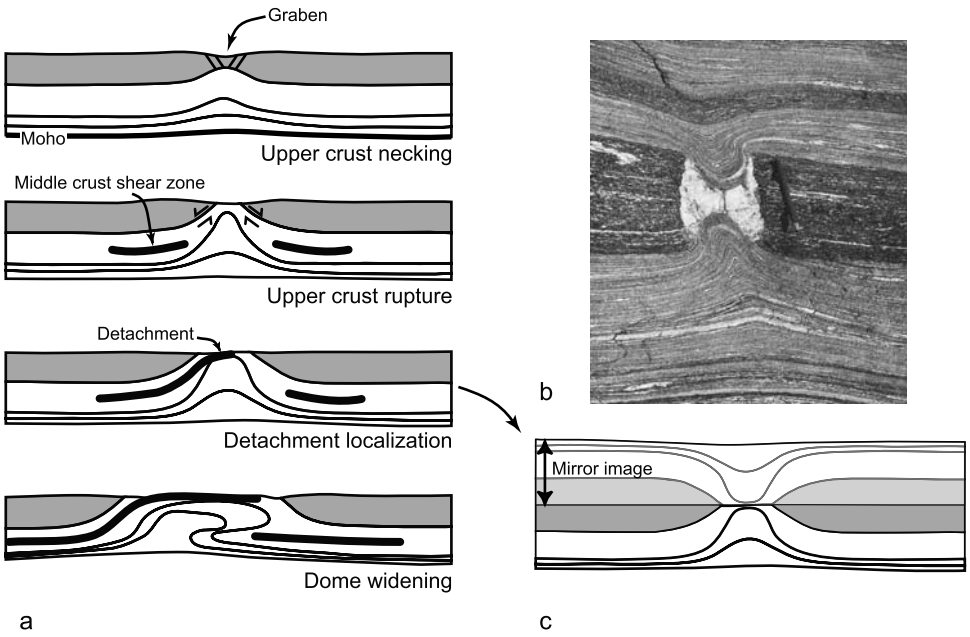

Figure 12. MCCs interpreted as a crustal-scale equivalent of scar folds between separating boudins. (a) Schematic evolution of a MCC development showing the formation of a crustal-scale dome between two boudins of the brittle crust. (b) Photograph of boudinage at an outcrop scale showing scar folds between boudins [*Passchier et al.*, 1990, Figure 4.16, p. 66] with kind permission of the authors and Springer Science and Business Media. (c) Model section with its mirror image superposed.

ment zone. At an initial Moho temperature of 830°C the sub-Moho olivine-controlled mantle has a strength slightly higher than that of the middle lower crust. The ductile crust deforms more easily than the mantle, a situation that favors a ductile crustal flow of channel type between the upper brittle crust and the lithospheric mantle. This gives rise to a velocity gradient close to the Moho and to the resulting highest shear strain intensities there. The late evolution, at large values of boundary displacement, does not show a significant propagation of the middle crust shear zone situated opposite to the moving boundary.

[75] At a Moho temperature of 1070°C, the detachment zone can localize on either of the dome limbs. The series of computed models show that at the highest velocities (1.32 to 2.66 cm a^{-1}) the detachment zone always localizes at the dome limb opposite to the moving boundary. At the lowest velocities (from 0.33 to 1.00 cm a^{-1}) no firm rule can be deduced; detachment zones are located on either of the dome limbs, without obvious reason.

[76] At high Moho temperatures and medium to high velocities, the middle crust shear zone located on the side of the dome opposite to the moving boundary, propagates across the dome toward the moving boundary during the late evolution of the MCCs development. Depending on the location of the detachment zone, two scenarios are possible (Figure 11). If the detachment zone is located on the dome limb opposite to the moving wall, the shear zone propagation results in a migration of the detachment zone within the dome. If the detachment zone is located on the dome limb closest to the moving boundary, the shear zone propagation produces a new detachment zone inside the dome, one with an opposite dip.

[77] This late stage structural evolution of domes has a substantial impact on the thermal structure. Before the propagation of the middle crust shear zone within the dome, the thermal structure is comparable to that observed in models with a Moho temperature of 830°C. The migration of the detachment zone or the creation of a new detachment zone inside the dome significantly changes the thermal structure and a new thermal subdome is created inside the original one.

[78] During the past two decades, detachment zones were most often considered as relatively steady state shear zones that accompany the development of MCCs from their inception to their mature development. Some observations, however, have suggested that a detachment zone can result from successive sequences of incisement or excisement [*Lister and Davis*, 1989], forming complex geometrical patterns. As discussed in the previous section, the detachment zones can be versatile in terms of their location and vergence (relative to the boundary displacement) and are not necessarily stable in time. A detachment zone can migrate in space or can die out and be replaced by a new one with an opposite vergence. Such features have not previously been reported. Future deep seismic studies across large MCCs should enable mapping their complex deep structure in sufficient detail.

7.5. A Simple Concept of MCCs

[79] Our models suggest that MCCs can be simply viewed as crustal-scale equivalents of the scar folds that result from "boudin" separation in the process of boudinage, as commonly observed in the field (Figures 12a and 12b) or in experiments [see *Price and Cosgrove*, 1990, chapter 16]. The comparison becomes even more obvious

when a model section showing the end of the symmetrical evolution is juxtaposed with its mirror image (Figure 12c). It must be noted that boudinage was already considered by *Davis* [1980] to explain the striking features of MCCs. However, in his concept of "megaboudinage," the MCCs themselves were compared to the boudins instead of the space between boudins.

[80] In all computed models, no detachment zone clearly localizes along one dome limb before the onset of the ductile crust exhumation; the pattern of deformation remains relatively symmetrical with opposite senses of shearing along the two dome limbs (Figure 12a). Depending on the input model parameters, the duration of the symmetrical evolution ranges from 3 to 20 Ma. The detachment zones result from a rather long duration of progressive deformation contrary to the most commonly accepted theories that postulate the existence of a shallow dipping detachment zone at crustal scale from the earliest stages of extension [*Wernicke*, 1981, 1985; *Spencer*, 1984; *Lister and Davis*, 1989]. The intense shearing that defines the detachment zone in our models is not related to any particular fault in the upper crust. It is, on the contrary, directly and solely related to the converging flow pattern in the ductile crust that accommodates the dome amplification and widening. Shear zones correspond to strong velocity gradients close to the brittle-ductile transition [*Tirel et al.*, 2004a, Figure 5]: flat-lying within the middle crust outside the dome, steeply dipping in the dome limbs, and flat-lying at the top of the exhumed dome.

[81] This nonconventional conception of extensional detachment zones mostly concerns the mylonitic part of the detachment zones that develop within rocks initially located below the brittle-ductile transition. In the classical models, detachment zones also involve a brittle part. In the "simple shear-type models" [*Wernicke*, 1981, 1985; *Lister and Davis*, 1989, *Livaccari et al.*, 1995], detachment faults initiate at a low-angle. In the "rolling hinge-type" models [*Buck*, 1988; *Wernicke and Axen*, 1988; *Axen and Bartley*, 1997] faults initiate at steep angles and are later rotated to lower dips on top of the low-angle mylonitic detachment. In our experiments, initial high normal faults evolve to lower angle due to the lower crustal flow exhumation, which fits better with the rolling hinge-type models. However, we do not use specific conditions which could allow rotation of the stress field and thus the formation of low-angle normal fault [*Wills and Buck*, 1997] as it is demonstrated in some field studies [*Lister and Davis*, 1989; *Livaccari et al.*, 1995]. Also, preexisting structures can modify significantly the distribution of stresses in the crust. For example, an earlier thrust fault can be reactivated as a detachment zone with a low angle as suggested by *Jolivet et al.* [2003]. In this study, deformation of the brittle crust is accommodated neither by a flat-lying normal fault, nor by a sequence of steep normal faults later rotated, but instead by conjugate normal faults defining a symmetrical graben. With increasing stretching the internal part of the graben becomes rapidly attenuated, allowing the initially ductile crust to exhume. This suggests that the particular pattern of faulting that contributes to the breakup of the upper crust is not a crucial point as long as it provides a gap for the exhumation of a metamorphic dome.

[82] The internal deep structure of our MCC models displays large-scale recumbent folding. This structural feature results directly from middle lower crustal flow which feeds the growing dome from below. This phenomenon has never been reported in previous studies and it is not unlikely that a thorough examination of deep seismic lines across large MCCs could also reveal them in the future. Moreover, in old deeply eroded mountain belts that have experienced late stage extension, such recumbent folds could possibly be identified in the field.

8. Conclusions

[83] The present numerical modeling of MCCs was carried out to study (1) the physical conditions that favor their development at the crustal and lithosphere scales and (2) their patterns of deformation at the crustal scale.

[84] The development of MCCs requires that the middle lower crust is weak enough to flow laterally, in order to feed an exhuming metamorphic dome. Dome exhumation in our models is always accompanied by a flat Moho geometry, even though the topography of the Moho is not constrained a priori and is allowed to vary. This is obtained for initial Moho temperatures of 800°C or higher. At these temperatures, the sub-Moho mantle and the middle lower crust both have small strengths and viscosities in the order of 10^{19}–10^{21} Pa s.

[85] The "geological window" for the development of MCCs, in addition to a Moho temperature of at least 800°C, requires a minimum crustal thickness of 45 km when considering the input parameters chosen for this study (Table 1). In other words, MCCs easily develop in continental crusts that are thickened and thermally softened. The critical times observed in our results are slightly influenced by the central granite-type anomaly used to localize strain but only during the first stages of exhumation.

[86] The deformation history of a MCC can be divided into two successive stages, here called "upper crust necking" and "dome amplification and widening". During the first stage, the deformation pattern is relatively symmetrical and is dominated by the formation of a graben in the upper crust. The transition to the second stage occurs when the upper brittle crustal layer is broken and the first layers originally located below the brittle-ductile transition arrive at the surface. Then, during the second stage, a metamorphic dome is progressively exhumed and the deformation pattern becomes strongly asymmetrical with the development of a detachment zone on one of the dome limbs. From this point of view, a MCC can be envisaged as a crustal-scale equivalent of the scar folds that fill the gap between separating boudins observed at the outcrop scale.

[87] Horizontal flow in the ductile crust, which accommodates the MCC development and occurs over distances several times larger than the width of the dome itself, is responsible for the development of horizontal shear zones in the middle crust and/or in the lower crust, above the Moho. Since the ductile crustal flow is a response to the horizontal pressure gradient created by local upper crustal thinning, the presence of a density anomaly does not modify the general two-stage process that characterizes the models presented here.

[88] Contrary to what is more generally acknowledged, the detachment zones do not initiate at the onset of extension but result from a progressive evolution. At early

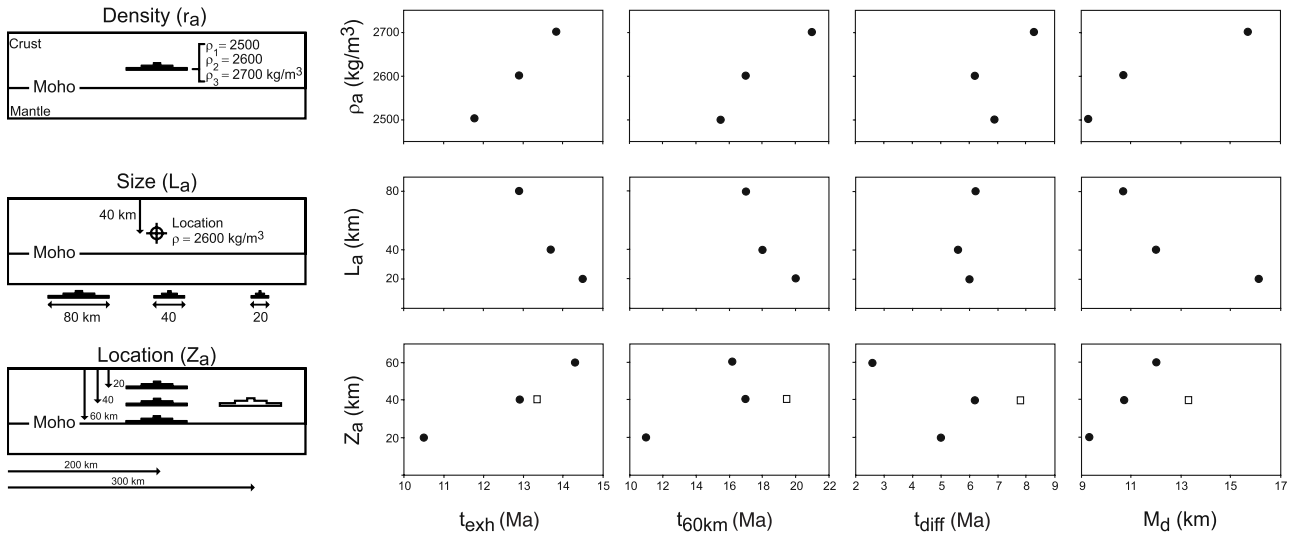

Figure A1. Effects of the anomaly properties and geometry (density, size, and location depth) on the onset of exhumation (t_{exh}), time necessary to exhume a 60 km wide dome (t_{60km}), t_{diff} (with $t_{diff} = t_{60km} - t_{exh}$), and Moho deflection ($M_d$).

stages of deformation, the highest strains are located at the base of the brittle crust graben and in the horizontal shear zones in the ductile crust. The horizontal shear zones then propagate upward along the two dome limbs toward the base of the opening graben. At the end of the first stage of the MCC development, the deformation pattern is almost symmetrical with no obvious detachment zone. At the next stage, the system rapidly becomes asymmetrical, with the localization of a detachment zone along one dome limb accommodating the further metamorphic dome widening.

[89] At initial Moho temperatures above ~1000°C, the location and vergence of detachment zones are more variable depending on the lateral boundary displacement conditions, and detachment formation can be unstable over time. At high values of dome widening, detachment zones can migrate in space or die out and be replaced by new ones with the opposite dip.

[90] Because of the 2 × 2 km resolution imposed by the size of model elements, the experiments presented in this paper do not reproduce deformation patterns related to the association of low-angle normal faults and ductile shear zones as commonly observed in field-scale cross sections. Finally, a parametric study has shown that the density-viscosity anomaly that we place in the ductile crust at the model center does not perturb significantly the extensional strain field associated with the MCCs. Rayleigh-Taylor instabilities, caused by the anomaly trigger strain localization at the onset of model deformation but do not alter the two-stage mechanism of the MCC development.

Appendix A: Localizing Anomaly in the Models

[91] In order to localize deformation at the model center, a compositional heterogeneity (anomaly) is placed in the ductile crust (Figure 1). The following study was carried out to determine the dynamic effect of the anomaly, in particularly of its density, size and location.

A1. Effects of the Properties of the Compositional Anomaly on Model Results

[92] To test the effects of variations in density (ρ_a), size (l_a) and location of the anomaly (z_a) on ductile crust exhumation (t_{exh}), dome growth (t_{diff}) and Moho deflection (M_d), a series of 9 model runs has been performed (Figure A1) with a model with a 60 km thick crust, where V = 0.66 cm a^{-1}, and T_{Mi} = 830°C (see Table 1). The parameter values used for the tests are ρ_a = 2500, 2600 and 2700 kg m^{-3}; l_a = 20, 40 and 80 km; z_a = 20, 40 and 60 km for an anomaly located at the model center; z_a = 40 km for an anomaly located at 300 km from the mobile boundary.

[93] Figure A1 shows the dependence of the onset of exhumation t_{exh} and the Moho deflection M_d on density, size and location of the anomaly. The onset of exhumation increases with increasing density or depth and with decreasing size of the anomaly. The largest effect is due to the location depth z_a, giving a variation of t_{exh} from 10 to 14 Ma. The Moho deflection increases with increasing size and depth and with decreasing density of the anomaly. The largest effect is due to either density or size, giving a variation of M_d from 9–10 to 16–17 km, i.e., by less than a factor of 2. The above results also show that the Moho deflection is strongly correlated with the timing of the exhumation (compare t_{exh} and M_d in Figure A1). The later the onset of exhumation, the more pronounced the Moho deflection.

[94] In the series of results presented in Figures 2 to 9 the anomaly is triangular in cross section (Figure 1a) with a basal width of l_a = 80 km and is located at the model center at a depth of 40 km. It has a density ρ_a = 2600 kg m^{-3} and the rheological properties of granite [*Kirby and Kronenberg*, 1987]. As demonstrated by the tests (Figure A1), such an anomaly tends to reduce both the onset of exhumation and the Moho deflection. These effects are smaller for models with higher initial Moho temperature, such as T_{Mi} = 1070°C and 1310°C.

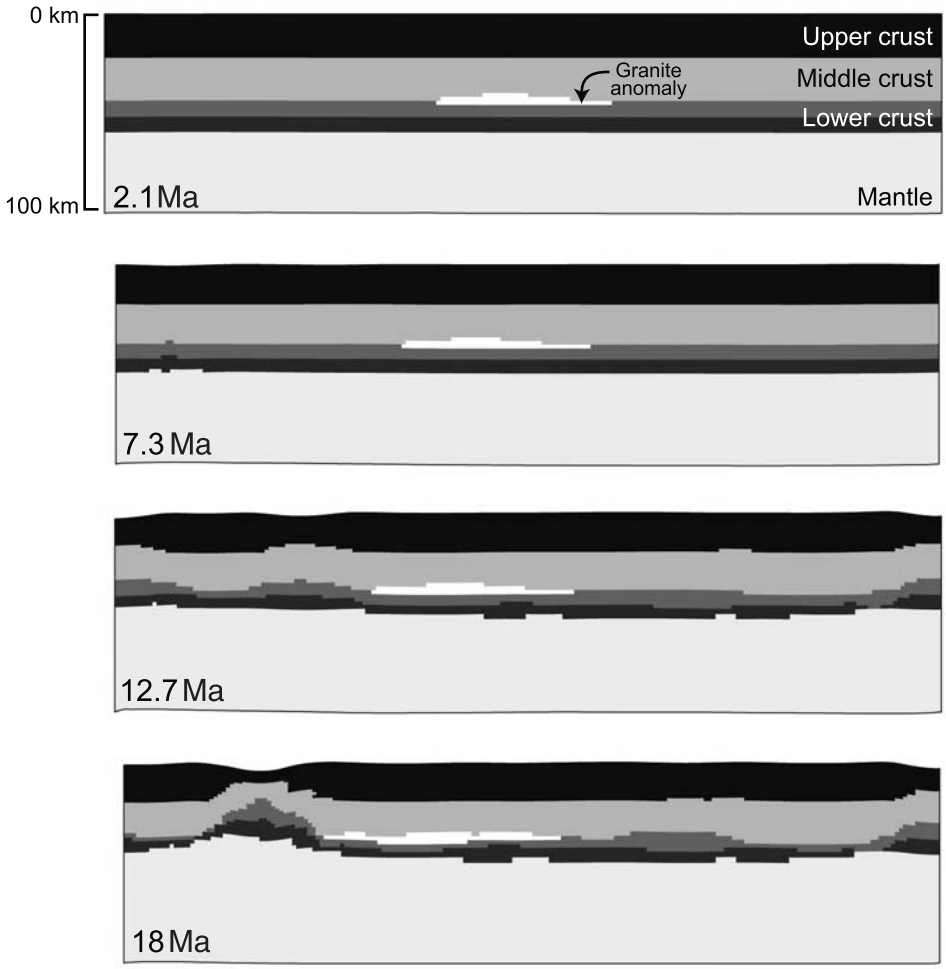

Figure A2. A model identical to the one represented in Figure 3 but with an anomaly without density contrast. Boundary velocity V = 0.66 cm a^{-1}. Initial Moho temperature T_{Mi} = 830°C. Even after 18 Ma, the central part of the model is only slightly deformed. Observed deformations are due to lateral boundaries, stronger near the moving one, on the left side.

A2. A Model Without Density Anomaly

[95] A model similar to the one of Figure 3 but without a density difference between the anomaly and its surrounding shows no deformation directly related to the anomaly, even after 18 Ma (Figure A2). The observed deformations are entirely due to lateral boundary effects, stronger to the left (near the mobile boundary) than to the right (near the free-slip boundary). A comparison with Figure 3 shows that the presence of a compositional anomaly localizes strain in the upper crust at early stages of development. At 7.3 Ma, upper crust necking is already close to rupture and at 13.3 Ma the process of ductile crust exhumation is advanced.

[96] The deformation localized near the left boundary leads to the necking and the ascent of the middle and lower crust; by horizontal flow is occurring due to the horizontal pressure gradient. This deformation could lead to a MCC development. Unfortunately, it begins close to the left border and quickly vanishes due to model grid remeshing. For this reason, the deformation has to be immediately triggered with an anomaly in the center of the box in order to set optimal conditions for observing the process of MCCs development.

[97] In the absence of a viscosity or density anomaly in the middle lower crust, the models yield a uniform extension at model scale with little or no local thinning of the upper brittle layer. Strain localization in the upper brittle layer and further development of MCCs are obtained only when a local density and/or viscosity anomaly is placed in the center of the model. The same conclusion was obtained by *Brun et al.* [1994] and later by *Tirel et al.* [2006] in comparable analogue experiments.

A3. Rayleigh-Taylor Instability Related to the Compositional Anomaly

[98] Another model run (similar to the one shown in Figure 3, but without displacement applied to the left boundary) has been carried out in order to test the effects of the density difference between the anomaly and its surroundings and of the resulting Rayleigh-Taylor-type instability (Figure A3).

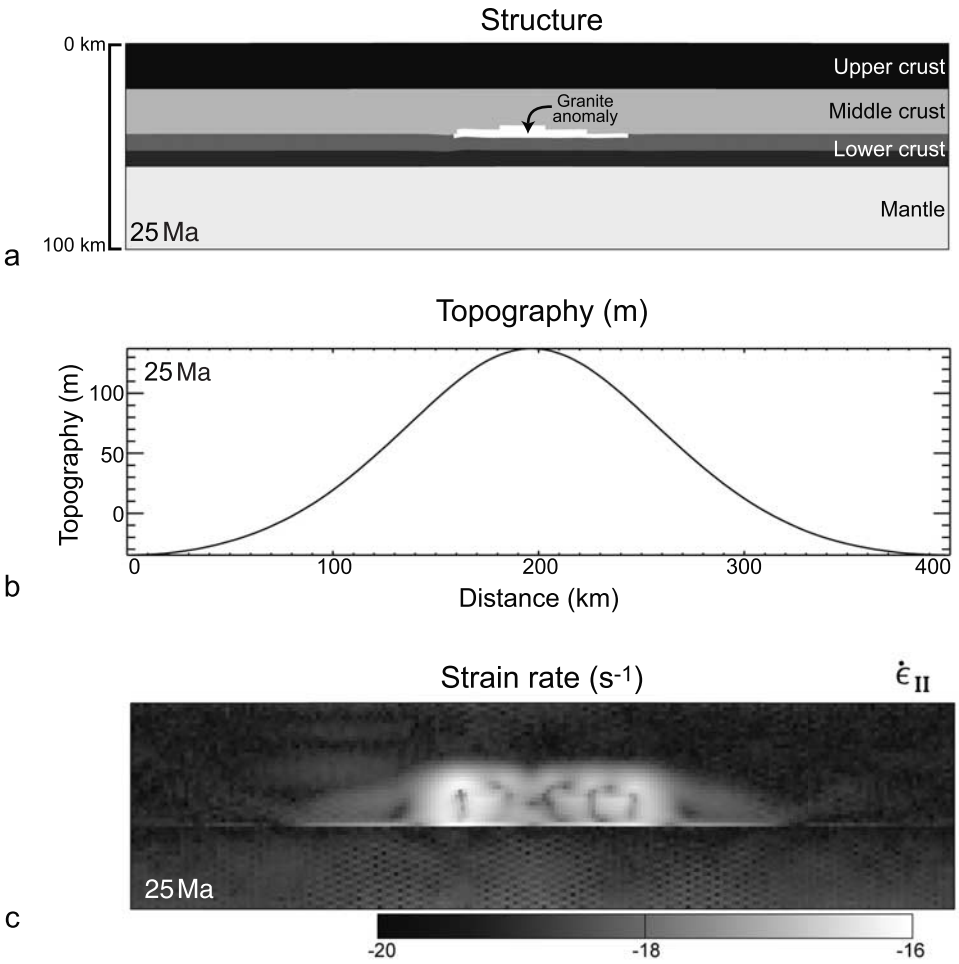

Figure A3. Rayleigh-Taylor effects due to the density anomaly only. Boundary velocity V = 0 cm a^{-1}. Initial Moho temperature T_{Mi} = 830°C. (a) Structure, (b) topography, and (c) strain rate at 25 Ma.

[99] After 25 Ma, only the right end of the anomaly has ascended by about 1.4 km (Figure A3a). The model topography (Figure A3b) shows a positive Gaussian-type shape with a maximal value of 140 m above the top of the anomaly. The pattern of strain rate (Figure A3c) indicates the presence of two convection cells. However, the observed range of strain rates, from 10^{-20} to 10^{-16} s^{-1}, is extremely low (at least 2 orders of magnitude below the bulk strain rate), which explains why the structure changed little in 25 Ma.

[100] For high initial Moho temperatures, T_{Mi} = 1070°C and 1310°C, and after 25 Ma, some parts of the anomaly have risen by up to 5 to 10 km, respectively. This does not, however, produce any deformation in the upper brittle crust.

[101] In summary, the Rayleigh-Taylor instability caused by the density anomaly has only minor direct effect. In an extensional environment, model runs with extension applied are sufficient to initiate strain localization.

[102] **Acknowledgments.** C. Tirel acknowledges the French Ministry of Education and Research for her thesis grant. This work was funded by the Institut Universitaire de France grant attributed to J.-P. Brun. E. Burov thanks Y. Podladchikov and A. Poliakov, who have codeveloped the kernel of PARAVOZ and generously shared their expertise on different stages of its further evolution. We thank D. Gapais, P. Gautier, and E. Hallot for discussions at various stages of the project and A. Kröner for his picture of boudinage. We are indebted to the Editor J. C. Mutter and C. Beaumont, G. Rosenbaum, R. Scott, and B. Hobbs for their constructive reviews that have greatly helped us to improve the manuscript. Special thanks to P. Ham and S. Lebedev for checking the English style. GMT software by *Wessel and Smith* [1995] was used for contour plots.

References

Abers, G. A., C. Z. Mutter, and J. Fang (1997), Shallow dips of normal faults during rapid extension: Earthquakes in the Woodlark-D'Entrecasteaux rift system, Papua New Guinea, *J. Geophys. Res.*, *102*, 15,301–15,317.

Allemand, P., and J.-P. Brun (1991), Width of continental rifts and rheological layering of the lithosphere, *Tectonophysics*, *188*, 63–69.

Allmendinger, R. W., K. Nelson, C. Potter, M. Barazangi, L. B. Brown, and J. E. Oliver (1987), Deep seismic reflection characteristics of the continental crust, *Geology*, *15*, 304–310.

Andersen, T. B. (1998), Extensional tectonics in the Caledonides of southern Norway, an overview, *Tectonophysics*, *285*, 333–351.

Andersen, T. B., B. Jamtveit, J. F. Dewey, and E. Swensson (1991), Subduction and eduction of continental crust; major mechanisms during continent-continent collision and orogenic extensional collapse, a model based on the South Norwegian Caledonides, *Terra Nova*, *3*, 303–310.

Anderson, E. M. (1951), *The Dynamics of Faulting*, Oliver and Boyd, Edinburgh, U. K.

Anderson, J. L., A. P. Barth, and E. D. Young (1988), Mid-crustal Cretaceous roots of Cordilleran metamorphic core complexes, *Geology*, *16*, 366–369.

Axen, G. J., and J. M. Bartley (1997), Field tests of rolling hinges: Existence, mechanical types, and implications for extensional tectonics, *J. Geophys. Res.*, *102*, 20,515–20,537.

Baldwin, S. L., G. S. Lister, E. J. Hill, D. A. Foster, and I. McDougall (1993), Thermochronologic constraints on the tectonic evolution of active metamorphic core complexes, D'Entrecasteaux Islands, Papua New Guinea, *Tectonics*, *12*, 611–628.

Bird, P. (1979), Continental delamination and the Colorado Plateau, *J. Geophys. Res.*, *86*, 4891–4903.
Block, L., and L. H. Royden (1990), Core complex geometries and regional scale flow in the lower crust, *Tectonics*, *9*, 557–567.
Bozkurt, E., and R. Oberhänsli (2001), Menderes Massif (western Turkey): Structural, metamorphic and magmatic evolution—A synthesis, *Int. J. Earth Sci.*, *89*, 679–708.
Brace, W. F., and D. L. Kohlstedt (1980), Limits on lithospheric stress imposed by laboratory experiments, *J. Geophys. Res.*, *85*, 6248–6252.
Brun, J.-P., and J. Van Den Driessche (1994), Extensional gneiss domes and detachment fault systems; structure and kinematics, *Bull. Soc. Geol. Fr.*, *165*, 519–530.
Brun, J.-P., D. Sokoutis, and J. Van Den Driessche (1994), Analogue modeling of detachment fault systems and core complexes, *Geology*, *22*, 319–322.
Buck, W. R. (1988), Flexural rotation of normal faults, *Tectonics*, *7*, 959–973.
Buck, W. R. (1991), Modes of continental lithospheric extension, *J. Geophys. Res.*, *96*, 20,161–20,178.
Burg, J. P., J. Van Den Driessche, and J.-P. Brun (1994), Syn to post-thickening extension in the Variscan Belt of western Europe: Modes and structural consequences, *Geol. Fr.*, *3*, 33–51.
Burov, E., and S. Cloetingh (1997), Erosion and rift dynamics: New thermomechanical aspects of post-rift evolution of extensional basins, *Earth Planet. Sci. Lett.*, *150*, 7–26.
Burov, E., and A. Poliakov (2001), Erosion and rheology controls on synrift and postrift evolution: Verifying old and new ideas using a fully coupled numerical model, *J. Geophys. Res.*, *106*, 16,461–16,481.
Burov, E., C. Jaupart, and L. Guillou-Frottier (2003), Ascent and emplacement of buoyant magma bodies in brittle-ductile upper crust, *J. Geophys. Res.*, *108*(B4), 2177, doi:10.1029/2002JB001904.
Burov, E. B., and L. Guillou-Frottier (1999), Thermomechanical behaviour of large ash flow calderas, *J. Geophys. Res.*, *104*, 23,081–23,109.
Byerlee, J. D. (1978), Friction of rocks, *Pure Appl. Geophys.*, *116*, 615–626.
Carter, T. J., B. P. Kohn, D. A. Foster, and A. J. W. Gleadow (2004), How the Harcuvar Mountains metamorphic core complex became cool: Evidence from apatite (U-Th)/He thermochronometry, *Geology*, *32*, 985–988.
Chéry, J. (2001), Core complex mechanics: From the Gulf of Corinth to the Snake Range, *Geology*, *29*, 439–442.
Clark, M. K., and L. H. Royden (2000), Topographic ooze: Building the eastern margin of Tibet by lower crustal flow, *Geology*, *28*, 703–706.
Crittenden, M. D., P. J. Coney, and G. H. Davis (Eds.) (1980), *Cordilleran Metamorphic Core Complexes*, *Mem. Geol. Soc. Am.*, *153*, 490 pp.
Cundall, P. A. (1989), Numerical experiments on localization in frictional materials, *Ing. Arch.*, *59*, 148–159.
Cundall, P. A. (1990), Numerical modelling of jointed and faulted rock, in *Mechanics of Jointed and Faulted Rock*, edited by A. Rossmanith, pp. 11–18, A. A. Balkema, Rotterdam, Netherlands.
Dallmeyer, R. D., A. W. Snoke, and E. H. McKee (1986), The Mesozoic-Cenozoic tectonothermal evolution of the Ruby mountains, East Humbolt range, Nevada: A cordilleran metamorphic core complex, *Tectonics*, *5*, 931–954.
Davis, G. A., and P. J. Coney (1979), Geological development of metamorphic core complexes, *Geology*, *7*, 120–124.
Davis, G. A., G. S. Lister, and S. J. Reynolds (1986), Structural evolution of the Whipple and South mountains shear zones, southwestern United States, *Geology*, *14*, 7–10.
Davis, G. H. (1980), Structural characteristics of metamorphic core complexes, southern Arizona, in *Cordilleran Metamorphic Core Complexes*, edited by M. C. Crittenden et al., *Mem. Geol. Soc. Am.*, *153*, 35–77.
Davis, G. H. (1983), Shear-zone model for the origin of metamorphic core complexes, *Geology*, *11*, 342–347.
Davis, G. H. (1987), Saguaro National Monument, Arizona: Outstanding display of the structural characteristics of metamorphic core complexes, in *Centennial Field Guide*, vol. 1, pp. 35–40, Cordilleran Sect., Geol. Soc. of Am., Boulder, Colo.
Dewey, J. F. (1988), Extensional collapse of orogens, *Tectonics*, *7*, 1123–1139.
Dewey, J. F., P. D. Ryan, and T. B. Andersen (1993), Orogenic uplift and collapse, crustal thickness, fabrics and facies changes: The role of eclogites, in *Magmatic Processes and Plate Tectonics*, edited by H. M. Prichard et al., *Geol. Soc. Spec. Publ.*, *76*, 325–343.
England, P. C., and M. Bickle (1984), Continental thermal and tectonic regimes during the Archaean, *J. Geol.*, *92*, 353–367.
England, P. C., and A. Thompson (1986), Some thermal and tectonic model for crustal melting in continental collision zones, in *Collision Tectonics*, edited by M. P. Cowards and A. C. Ries, *Geol. Soc. Spec. Publ.*, *19*, 83–94.
Gaudemer, Y., C. Jaupart, and P. Tapponnier (1988), Thermal control on post-orogenic extension in collision belts, *Earth Planet. Sci. Lett.*, *89*, 48–62.
Gautier, P., and J.-P. Brun (1994a), Crustal-scale geometry and kinematics of late-orogenic extension in the central Aegean (Cyclades and Evvia Island), *Tectonophysics*, *238*, 399–424.
Gautier, P., and J.-P. Brun (1994b), Ductile crust exhumation and extensional detachments in the central Aegean (Cyclades and Evvia islands), *Geodin. Acta*, *7*, 57–85.
Gautier, P., M. Ballèvre, J.-P. Brun, and L. Jolivet (1990), Extension ductile et bassins sédimentaires mio-pliocènes dans les Cyclades (îles de Naxos et Paros), *C. R. Acad. Sci.*, *310*, 147–153.
Gautier, P., J.-P. Brun, and L. Jolivet (1993), Structure and kinematics of upper Cenozoic extensional detachment on Naxos and Paros (Cyclades Islands, Greece), *Tectonics*, *12*, 1180–1194.
Gerbault, M., A. Poliakov, and M. Daignieres (1998), Prediction of faulting from the theories of elasticity and plasticity: What are the limits?, *J. Struct. Geol.*, *20*, 301–320.
Gerbault, M., E. B. Burov, A. N. B. Poliakov, and M. Dagnières (1999), Do faults trigger folding in the lithosphere?, *Geophys. Res. Lett.*, *26*, 271–274.
Gerya, T. V., W. V. Maresch, A. P. Willner, D. D. Van Reenen, and C. A. Smit (2001), Inherent gravitational instability of thickened continental crust regionally developed low- to medium-pressure granulite facies metamorphism, *Earth Planet. Sci. Lett.*, *190*, 221–235.
Gerya, T. V., D. A. Yuen, and W. V. Maresch (2004), Thermomechanical modelling of slab detachment, *Earth Planet. Sci. Lett.*, *226*, 101–116.
Gessner, K., C. Wijns, and L. Moresi (2007), Significance of strain localization in the lower crust for structural evolution and thermal history of metamorphic core complexes, *Tectonics*, *26*, TC2012, doi:10.1029/2004TC001768.
Gueydan, F., Y. M. Leroy, L. Jolivet, and P. Agard (2003), Analysis of continental midcrustal strain localization induced by microfracturing and reaction-softening, *J. Geophys. Res.*, *108*(B2), 2064, doi:10.1029/2001JB000611.
Gueydan, F., Y. M. Leroy, and L. Jolivet (2004), Mechanics of low-angle extensional shear zones at the brittle-ductile transition, *J. Geophys. Res.*, *109*, B12407, doi:10.1029/2003JB002806.
Hamilton, W. (1988), Extensional faulting in the Death Valley region, *Geol. Soc. Am. Abstr. Programs*, *20*, 165–166.
Hauser, E., C. Potter, T. Hauge, S. Burgess, S. Burtch, J. Murtschler, R. Allmendinger, L. Brown, S. Kaufman, and J. Oliver (1987), Crustal structure of eastern Nevada from COCORP deep seismic reflection data, *Geol. Soc. Am. Bull.*, *99*, 833–844.
Hill, R. I., H. Campbell, G. F. Davies, and R. W. Griffiths (1992), Mantle plumes and continental tectonics, *Science*, *256*, 186–192.
Hubbert, M. K. (1951), Mechanical basis for certain geological structures, *Geol. Soc. Am. Bull.*, *62*, 355–372.
Hyndman, R. D., C. A. Currie, and S. P. Mazzotti (2005), Subduction zone backarcs, mobile belts, and orogenic heat, *GSA Today*, *15*, 4–10.
John, B. E., and K. A. Howard (1995), Rapid extension recorded by cooling-age patterns and brittle deformation, Naxos, Greece, *J. Geophys. Res.*, *100*, 9969–9979.
Jolivet, L. (2001), A comparison of geodetic and finite strain in the Aegean, geodynamic implications, *Earth Planet. Sci. Lett.*, *187*, 95–104.
Jolivet, L., J. P. Brun, P. Gautier, S. Lallemant, and M. Patriat (1994), 3D-kinematics of extension in the Aegean region from the early Miocene to the present; insights from the ductile crust, *Bull. Soc. Geol. Fr.*, *165*, 195–209.
Jolivet, L., et al. (1998), Midcrustal shear zones in postorogenic extension: Example from the northern Tyrrhenian Sea, *J. Geophys. Res.*, *103*, 12,123–12,160.
Jolivet, L., C. Faccenna, B. Goffé, E. Burov, and P. Agard (2003), Subduction tectonics and exhumation of high-pressure metamorphic rocks in the Mediterranean orogens, *Am. J. Sci.*, *303*, 353–409.
Kirby, S. H., and A. K. Kronenberg (1987), Rheology of the lithosphere: Selected topics, *Rev. Geophys.*, *25*, 1219–1244.
Kruger, J. M., and R. A. Johnson (1994), Raft model of crustal extension: Evidence from seismic reflection data in southeast Arizona, *Geology*, *22*, 351–354.
Lavier, L. L., W. R. Buck, and A. N. B. Poliakov (1999), Self-consistent rolling-hinge model for the evolution of large-offset low-angle normal faults, *Geology*, *27*, 1127–1130.
Lavier, L. L., W. R. Buck, and A. N. B. Poliakov (2000), Factors controlling normal fault offset in an ideal brittle layer, *J. Geophys. Res.*, *105*, 23,431–23,442.
Lefort, J.-P., M. Cuney, C. Deniel, C. France-Lanord, S. M. F. Shepard, B. N. Upreti, and P. Vidal (1987), Crustal generation of the Himalayan leucogranites, *Tectonophysics*, *134*, 39–57.

Le Pichon, X. (1982), Land-locked oceanic basins and continental collision: The eastern Mediterranean as a case example, in *Mountain Building Processes*, edited by K. J. Hsü, pp. 201–211, Academic, London.

Le Pourhiet, L., E. Burov, and I. Moretti (2004), Rifting through a stack of inhomogeneous thrusts (the dipping pie concept), *Tectonics*, *23*, TC4005, doi:10.1029/2003TC001584.

Lister, G. S., and S. L. Baldwin (1993), Plutonism and the origin of metamorphic core complexes, *Geology*, *21*, 607–610.

Lister, G. S., and G. A. Davis (1989), The origin of metamorphic core complexes and detachment faults formed during Tertiary continental extension in the northern Colorado River region, U.S.A., *J. Struct. Geol.*, *11*, 65–94.

Lister, G. S., G. Banga, and A. Feenstra (1984), Metamorphic core complexes of Cordilleran type in the Cyclades, Aegean Sea, Greece, *Geology*, *12*, 221–225.

Livaccari, R. F., J. W. Geissman, and S. J. Reynolds (1995), Large-magnitude extensional deformation in the South Mountains metamorphic core complex, Arizona: Evaluation with paleomagnetism, *Geol. Soc. Am. Bull.*, *107*, 877–894.

Makris, J. (1978), The crust and upper mantle of the Aegean region from deep seismic soundings, *Tectonophysics*, *46*, 269–284.

Martinez-Martinez, J. M., J. I. Soto, and J. C. Balanya (2004), Elongated domes in extended orogens: A mode of mountain uplift in the Betics (southeast Spain), in *Gneiss Domes in Orogeny*, edited by D. L. Whitney et al., *Spec. Pap. Geol. Soc. Am.*, *380*, 243–265.

McCarthy, J., S. P. Larkin, G. S. Fuis, R. W. Simpson, and K. A. Howard (1991), Anatomy of a metamorphic core complex: Seismic refraction/wide-angle reflection profiling in southeastern California and western Arizona, *J. Geophys. Res.*, *96*, 12,259–12,291.

McClusky, S., et al. (2000), Global Positioning System constraints on plate kinematics and dynamics in the eastern Mediterranean and Caucasus, *J. Geophys. Res.*, *105*, 5695–5719.

McKenzie, D., and J. Jackson (2002), Conditions for flow in the continental crust, *Tectonics*, *21*(6), 1055, doi:10.1029/2002TC001394.

McKenzie, D., F. Nimmo, J. A. Jackson, P. B. Gans, and E. L. Miller (2000), Characteristics and consequences of flow in the lower crust, *J. Geophys. Res.*, *105*, 11,029–11,046.

Melosh, H. J. (1990), Mechanical basis for low-angle normal faulting in the Basin and Range province, *Nature*, *343*, 331–335.

Miller, E. L., P. B. Gans, and J. Garing (1983), The Snake Range décollement: An exhumed mid-tertiary ductile-brittle transition, *Tectonics*, *2*, 239–263.

Norlander, B. H., D. L. Whitney, C. Teyssier, and O. Vanderhaeghe (2002), Partial melting and decompression of the Thor-Odin dome, Shuswap metamorphic core complex, Canadian Cordillera, *Lithos*, *61*, 103–125.

Norton, M. G. (1986), Late Caledonides extension in western Norway: A response to extreme crustal thickening, *Tectonics*, *5*, 195–204.

Ord, A. (1991), Deformation of rock: A pressure-sensitive, dilatant material, *Pure Appl. Geophys.*, *137*, 337–366.

Passchier, C. W., J. S. Myers, and A. Kröner (1990), *Field Geology of High-Grade Gneiss Terrains*, 150 pp., Springer, Berlin.

Poliakov, A. N. B., P. Cundall, Y. Podlachikov, and V. Laykhovsky (1993), An explicit inertial method for the simulation of visco-elastic flow: An evaluation of elastic effects on diapiric flow in two and three-layers models, in *Flow and Creep in the Solar System: Observations, Modeling and Theory*, *NATO ASI Ser., Ser. E*, vol. 391, edited by D. B. Stone and S. K. Runcorn, pp. 175–195, Kluwer, Dordrecht, Netherlands.

Price, N. J., and J. W. Cosgrove (1990), *Analysis of Geological Structures*, Cambridge Univ. Press, Cambridge, U. K.

Ranalli, G. (1997), Rheology of the lithosphere in space and time, in *Orogeny Through Time*, edited by J. P. Burg and M. Ford, *Geol. Soc. Spec. Publ.*, *121*, 19–37.

Ranalli, G., and D. C. Murphy (1987), Rheological stratification of the lithosphere, *Tectonophysics*, *132*, 281–295.

Regenauer-Lieb, K., R. Weinberg, and G. Rosenbaum (2006), The effect of energy feedbacks on continental strength, *Nature*, *442*, 67–70.

Rehrig, W. A., and S. J. Reynolds (1980), Geologic and geochronologic reconnaissance of a northwest-trending zone of metamorphic core complexes in southern and western Arizona, in *Cordilleran Metamorphic Core Complexes*, edited by M. C. Crittenden et al., *Mem. Geol. Soc. Am.*, *153*, 131–158.

Reynolds, S. J., and W. A. Rehrig (1980), Mid-Tertiary plutonism and mylonitization, South Mountains, central Arizona, in *Cordilleran Metamorphic Core Complexes*, edited by M. C. Crittenden et al., *Mem. Geol. Soc. Am.*, *153*, 159–175.

Rigo, A., H. Lyon-Caen, R. Armijo, A. Deschamps, D. Hatzfeld, K. Makropoulos, P. Papadimitriou, and I. Kassaras (1996), A microseismic study in the western part of the Gulf of Corinth (Greece): Implications for large-scale normal faulting mechanisms, *Geophys. J. Int.*, *126*, 663–688.

Roman-Berdiel, T., D. Gapais, and J.-P. Brun (1995), Analogue models of laccolith formation, *J. Struct. Geol.*, *17*, 1337–1346.

Rosenbaum, G., K. Regenauer-Lieb, and R. Weinberg (2005), Continental extension: From core complexes to rigid block faulting, *Geology*, *33*, 609–612.

Sachpazi, M., A. Hirn, A. Nercessian, F. Avedik, J. Mc Bride, M. Loucoyannakis, R. Nicolich, and STREAMERS-PROFILES Group (1997), A first coincident normal-incidence and wide-angle approach to studying the extending Aegean crust, *Tectonophysics*, *270*, 301–312.

Scaillet, B., A. Pêcher, P. Rochette, and M. Champenois (1995), The Gangotri granite (Garhwal Himalaya): Laccolithic emplacement in an extending collisional belt, *J. Geophys. Res.*, *100*, 585–607.

Sonder, L. J., P. C. England, B. P. Wernicke, and R. L. Christiansen (1987), A physical model for Cenozoic extension of western North America, in *Continental Extensional Tectonics*, edited by M. P. Coward et al., *Geol. Soc. Spec. Publ.*, *28*, 187–201.

Spencer, J. E. (1984), Role of tectonic denudation in the warping and uplift of low-angle normal faults, *Geology*, *12*, 95–98.

Tirel, C., J.-P. Brun, and E. Burov (2004a), Thermomechanical modeling of extensional gneiss domes, in *Gneiss Domes in Orogeny*, edited by D. L. Whitney et al., *Spec. Pap. Geol. Soc. Am.*, *380*, 67–78.

Tirel, C., F. Gueydan, C. Tiberi, and J.-P. Brun (2004b), Aegean crustal thickness inferred from gravity inversion: Geodynamical implications, *Earth Planet. Sci. Lett.*, *228*, 267–280.

Tirel, C., J.-P. Brun, and D. Sokoutis (2006), Extension of thickened and hot lithospheres: Inferences from laboratory modeling, *Tectonics*, *25*, TC1005, doi:10.1029/2005TC001804.

Turcotte, D. L., and G. Schubert (2002), *Geodynamics*, Cambridge Univ. Press, Cambridge, U. K.

Van Den Driessche, J., and J.-P. Brun (1989), Un modèle cinématique de l'extension paléozoique supérieure dans le sud du Massif Central, *C. R. Acad. Sci.*, *309*, 1607–1613.

Van Den Driessche, J., and J.-P. Brun (1991), Tectonic evolution of the Montagne Noire (French Massif Central): A model of extensional gneiss dome, *Geodin. Acta*, *5*, 85–99.

Vanderhaeghe, O., C. Teyssier, I. McDougall, and W. J. Dunlap (2003), Cooling and exhumation of the Shuswap Metamorphic Core Complex constrained by $^{40}Ar/^{39}Ar$ thermochronology, *Geol. Soc. Am. Bull.*, *115*, 200–216.

Vermeer, P. A., and R. De Borst (1984), Non-associated plasticity for soils, concrete and rock, *Heron*, *29*(3), 3–64.

Vissers, R. L. M., J. P. Platt, and D. van der Wal (1995), Late orogenic extension of the Betic Cordillera and the Alboran Domain: A lithospheric view, *Tectonics*, *14*, 786–803.

Wakabayashi, J. (2004), Tectonic mechanisms associated with P-T paths of regional metamorphism: Alternatives to single-cycle thrusting and heating, *Tectonophysics*, *392*, 193–218.

Wdowinski, S., and G. J. Axen (1992), Isostatic rebound due to tectonic denudation: A viscous flow model of a layered lithosphere, *Tectonics*, *11*, 303–315.

Wernicke, B. (1981), Low-angle normal faults in the Basin and Range Province: Nappe tectonics in an extending orogen, *Nature*, *291*, 645–648.

Wernicke, B. (1985), Uniform-sense normal simple shear of the continental lithosphere, *Can. J. Earth Sci.*, *22*, 108–125.

Wernicke, B. (1990), The fluid crustal layer and its implications for continental dynamics, in *Exposed Cross-Sections of the Continental Crust*, edited by M. H. Salisbury and D. M. Fountain, pp. 509–544, Kluwer Acad., Norwell, Mass.

Wernicke, B., and G. J. Axen (1988), On the role of isostasy in the evolution of normal fault systems, *Geology*, *16*, 848–851.

Wessel, P., and W. H. F. Smith (1995), New version of the generic mapping tools, *Eos Trans. AGU*, *76*, 329.

Westaway, R. (1999), The mechanical feasibility of low-angle normal faulting, *Tectonophysics*, *308*, 407–443.

Wijns, C., R. Weinberg, K. Gessner, and L. Moresi (2005), Mode of crustal extension determined by rheological layering, *Earth Planet. Sci. Lett.*, *236*, 120–134.

Wills, S., and W. R. Buck (1997), Stress-field rotation and rooted detachment faults: A Coulomb failure analysis, *J. Geophys. Res.*, *102*, 20,503–20,514.

J.-P. Brun, Géosciences Rennes, UMR 6118, CNRS, Université de Rennes 1, Avenue du General Leclerc, F-35042 Rennes, France.

E. Burov, Laboratoire de Tectonique, UMR 7072, CNRS, Université Pierre et Marie Curie, 4 place Jussieu, Tour 46, etage 2, col 46-00, F-75252 Paris Cedex 05, France.

C. Tirel, Faculty of Geosciences, Tectonophysics, Utrecht University, Budapestlaan 4, NL-3584 CD Utrecht, Netherlands. (c.tirel@geo.uu.nl)